Giant seabed polygons and underlying polygonal faults in the Caribbean Sea as markers of the sedimentary cover extension in the Grenada Basin

Aurelien Gay[1], Crelia Padron[2], Solene Meyer[3], Daniel Beaufort[4], Émilien Oliot[5], Serge E. Lallemand[6], Boris Marcaillou[7], Mélody Philippon[8], Jean-Jacques Cornée[9], Franck A. Audemard[10], Jean-Frédéric Lebrun[11], Frauke Klingelhoefer[12], Bernard Mercier de Lepinay[13], Philippe Munch[14], Clément Garrocq[8], Milton Boucart[15], Mireille Laigle[16], and Laure Schenini[17]

[1]Université de Montpellier, Université des Antilles
[2]Ifremer
[3]University of Montpellier
[4]Université de Poitiers
[5]UMR 5243 Géosciences Montpellier, CNRS, Université de Montpellier, 34095, Montpellier Cedex 05, France
[6]CNRS, Universite Montpellier
[7]Université Côte d'Azur, CNRS, Observatoire de la Côte d'Azur, IRD, Geoazur
[8]Géosciences Montpellier
[9]University of Montpellier, France
[10]FUNVISIS
[11]Université des Antilles
[12]IFREMER
[13]CNRS Université Côte d'Azur
[14]Geosciences Montpellier
[15]Université Côte d'Azur
[16]Université Nice Sophia Antipolis
[17]Université Côte d'Azur, CNRS, Observatoire de la Côte d'Azur, IRD, Géoazur, v

November 26, 2022

Abstract

Based on an extensive seismic and multibeam dataset, 1-5 km wide giant polygons were identified at the bottom of the Grenada basin, covering a total area of ~55000 km². They represent the top part of an active underlying polygonal fault system due to the volumetric contraction of clay- and smectite-rich sediments during burial. To date, this is the widest area of outcropping polygonal faults ever found on Earth. The seabed polygons are bounded by rectilinear ~1000-1500 m wide and ~10-60 m deep furrows, depending on the location in the basin. They are relatively regular in the north Grenada Basin, whereas they are getting longer and more elongated in the south Grenada Basin. The polygonal faults consist in a set of discrete normal faults affecting a 700 to 1200 m thick interval, initiated in the shallow sub-surface at the transition between Early to Middle Pliocene and then having propagated both upward and downward during sedimentation. The centre-to-centre method has been applied to determine the local ellipse of strains, providing a major orientation for extension needed for polygons to initiate. In the north,

the minor axes are oriented N40°, indicating a general NE-SW extension of the upper part of the sedimentary cover consistent with the forearc/backarc regional extension. In the south Grenada Basin, minor axes are progressively turning towards the south, pointing out the actual maximum subsidence point. This implies that seabed polygonal faults could thus be indicative of the present-day (or recent) strain state within the upper sedimentary column.

Giant seabed polygons and underlying polygonal faults in the Caribbean Sea as markers of the sedimentary cover extension in the Grenada Basin

A. Gay[1,*], C. Padron[2,3], S. Meyer[1,4], D. Beaufort[5], E. Oliot[1], S. Lallemand[1], B. Marcaillou[4], M. Philippon[1], J-J. Cornée[1], F. Audemard[6], J-F. Lebrun[1], F. Klingelhoefer[3], B. Mercier de Lepinay[4], P. Münch[1], C. Garrocq[1], M. Boucart[1,4], M. Laigle[4], L. Schenini[4] and the GARANTI cruise team.

1 Géosciences Montpellier, CNRS, Université de Montpellier, Université des Antilles, Place Eugène Bataillon, 34095 Montpellier, France

2 Departamento de Ciencias de la Tierra, Universidad Simón Bolívar (USB), Caracas, Venezuela.

3 Géosciences Marines, Ifremer, ZI de la Pointe du Diable, CS 10070, 29280 Plouzané, France

4 Géoazur, Université Côte d'Azur, CNRS, IRD, Observatoire de la Côte d'Azur, Géoazur, 250 Avenue Albert Einstein, 06560 Valbonne, France

5 Université de Poitiers, IC2MP - UMR 7285 - CNRS, Rue Michel Brunet, F-86073 Poitiers cedex 9, France

6 Universidad Nacional de San Luis, San Luis, Argentina

* corresponding author: aurelieng.gay@umontpellier.fr

Key points:

> Seabed giant polygons were identified in the Grenada Basin, covering the widest area (55000 km²) ever found on Earth

> The local ellipse of strains provided major orientations for extension needed for polygons to initiate

> Polygonal faults orientations are indicative of the modern strain state in the upper sedimentary column, defining two major tectonic domains

Abstract

Based on an extensive seismic and multibeam dataset, 1-5 km wide giant polygons were identified at the bottom of the Grenada basin, covering a total area of ~55000 km². They represent the top part of an active underlying polygonal fault system due to the volumetric contraction of clay- and smectite-rich sediments during burial. To date, this is the widest area of outcropping polygonal faults ever found on Earth. The seabed polygons are bounded by rectilinear ~1000-1500 m wide and ~10-60 m deep furrows, depending on the

location in the basin. They are relatively regular in the north Grenada Basin, whereas they are getting longer and more elongated in the south Grenada Basin. The polygonal faults consist in a set of discrete normal faults affecting a 700 to 1200 m thick interval, initiated in the shallow sub-surface at the transition between Early to Middle Pliocene and then having propagated both upward and downward during sedimentation. The centre-to-centre method has been applied to determine the local ellipse of strains, providing a major orientation for extension needed for polygons to initiate. In the north, the minor axes are oriented N40°, indicating a general NE-SW extension of the upper part of the sedimentary cover consistent with the forearc/backarc regional extension. In the south Grenada Basin, minor axes are progressively turning towards the south, pointing out the actual maximum subsidence point. This implies that seabed polygonal faults could thus be indicative of the present-day (or recent) strain state within the upper sedimentary column.

Introduction

Polygonal fault systems (PFS) have been recognised in many basins worldwide (Klitgord & Grow, 1980; Clausen & Korstgård, 1993; Cartwright, 1994; Oldham & Gibbins, 1995; Lonergan & Cartwright, 1998; Clausen et al., 1999; Gay et al., 2004; Hansen et al., 2004; Gay et al., 2007; Gay et al, 2009; He et al., 2010; Sun et al., 2010; Cartwright, 2011, Laurent et al., 2012; Ghalayini & Eid, 2020). They are a special type of non-tectonic normal faults forming polygons in plane view and prisms in 3D, similar to other environments, such as thermal contraction of cooling lavas, ice-wedge polygons (Lachenbruch, 1962) or desiccation cracks (Weinberger, 1999).

Four main hypotheses are proposed to explain the PFS formation: i) synersis related to colloidal properties of fine-grained sediments (Dewhurst et al., 1999), ii) density inversions and associated hydrofracturing (Watterson et al., 2000), iii) smectite-rich clays causing residual friction at low burial depth (Goulty, 2002; 2008) and iv) grain dissolution in uncemented media inducing a decrease in horizontal stress that leads to shear failure and shear strain localization (Shin et al., 2008; 2010). Other mechanisms different from lithology variation have been referenced in the literature as responsible for polygonal fault initiation, propagation or reactivation, such as sediment loading (Gay et al., 2007). In any case, this kind of shrinkage is due to diagenetic reactions in the host-rock unit during early burial causing volumetric contraction of fine-grained clay-rich sediments accommodated by small scale normal faults (Gay et al., 2004; Neagu et al., 2010; Ireland et al., 2011; Davies et al., 2009; Wrona et al., 2017).

PFS are usually interpreted as layer-confined because they occur within sub-horizontal intervals, a few hundreds of m thick, associated with lithological variations of the host sediments. They do not abruptly end at a specific stratigraphical horizon and they can locally connect to major faults structuring the basin (Gay et al., 2007). Some of these faults almost reach the modern seabed, thus representing the top of a modern or recently active polygonal fault system (Hansen et al., 2005; Ireland et al., 2011). Even if a polygonal fault interval (PFI) is generally buried from a few tens of meters to hundreds of meters, only a few examples have been reported outcropping at the present-day seabed such as in the Hatton Basin (Berndt et al., 2012).

In the investigated area, extending from the Saba Bank southwest of Virgin Islands in the north Grenada Basin (NGB) to the south Grenada Basin (SGB) west off Grenada island, the Grenada Basin is in the backarc basin of the subducting North American Plate beneath the Caribbean Plate (**Fig. 1**). Giant polygons, 1 to 5 km wide, have been identified outcropping at the seabed during the GARANTI Cruise in May-June 2017. They cover the widest area of outcropping polygonal faults ever found on Earth, with a surface of ~55000 km². They are directly linked to a unique underlying 1000 m thick PFI that thins towards the modern volcanic arc where it abruptly ends and towards the North where sedimentary sequences are getting thinner. However, the PFI also extends towards the Venezuela Basin covering a total area of ~75000 km² in the study area, meaning that its total extent is probably much more.

Recent studies have attempted to link PFS with structural context using topology of the faults (Morley & Binazirnejad, 2020 and references therein) and/or rose diagram orientations (Jimahantakul et al., 2020 and references therein). Even if the fault pattern can be influenced by the slope of underlying units, causing different amounts of horizontal stress anisotropy within the faulted units (Gay et al., 2004; Li et al., 2020), the fault orientations are generally used as a direct marker of extension related to local paleo-stress fields during PFS formation (Laurent et al., 2012, Ho et al., 2018). The large extent of acquired data from north to south in the Grenada Basin gives the opportunity to investigate whether these polygonal faults are related to the current state of stress in the sedimentary cover by using a novel approach involving the centre-to-centre method. This method applied to adjacent polygons provided unexpected results with the evolving orientation of the sedimentary cover extension in the entire Grenada Basin.

Figure 1: Regional map of the eastern Caribbean Sea displaying the extension of giant seabed polygons (green line) and underlying polygonal faults (blue line) developing in the north Grenada Basin (NGB) and the south Grenada Basin (SGB). The multibeam bathymetry data and corresponding MCS profiles (noted GA-) were acquired during the GARANTI cruise in 2017. Additional seismic profiles (BOL30, 124VB-11 and 124VB-12) were used to extend the interpretation in the south. The grab cores GR-07 and GR-08 were collected within the area of seabed polygons. The shaded relief map is extracted from GEBCO datasets.
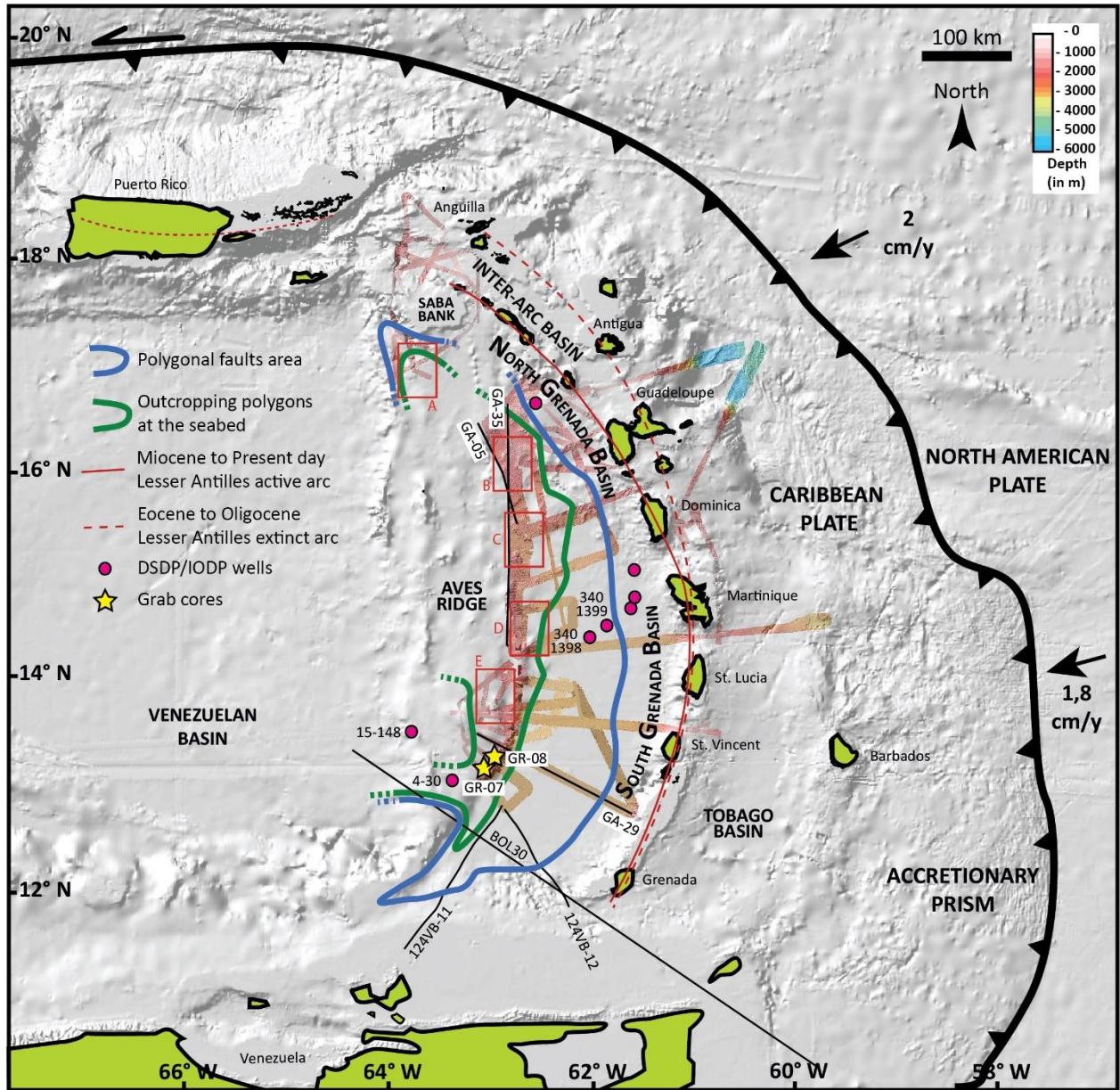
Data and methods

Deep-penetration multichannel seismic reflection (MCS) data were acquired onboard *R/V L'Atalante* during the GARANTI cruise in 2017 (Lebrun & Lallemand, 2017) (**Fig. 1**). MCS data were collected using a 6473 in^3 airgun array of 16 seismic sources emitting signals with a 9-40 Hz frequency range, and a 4.5 km long, 720-channel solid streamer. The data were quality-controlled and binned in common midpoint (CMP) gathers every 12.5 meters using the SolidQC software of IFREMER and they were processed using the Geovation Software. EM122 multibeam bathymetric data and high-resolution CHIRP profiles were also recorded along all seismic profiles. Additional profiles BOL30, 124VB-11 and 124VB-12 were used to connect our interpretation with previous studies in the SGB (**Fig. 1**).

Clay mineralogy of the core samples GR-07 and GR-08 collected during the GARANTI cruise (**Fig. 1**) was determined from X-ray diffractograms of oriented powder mounts of the bulk material and the less than 2 μm

112 granulometric fraction which is usually considered as representative of the clay fraction of sedimentary rocks.
113 Oriented preparations are a prerequisite for a detailed characterization of the d00ℓ reflections of phyllosilicates.
114 The disaggregation of the bulk sediments and the dispersion of clay particles was made by ultrasonic treatment
115 in distilled water without any preliminary grinding to strongly limit the contamination with fine grained
116 fragments of detrital minerals. The less than 2 μm fraction was then extracted from the previous suspension
117 by centrifugation. X-ray diffractograms were acquired on a Bruker D8 Advance diffractometer (40 kV and 40
118 mA) coupled with a copper anticathode (Cu Kα^{1+2} radiation) in the 2-30º2Θ angular range with 0.02°2Θ steps
119 and a counting time of 2 seconds per step. Relative humidity was not controlled during data acquisition.

120 SEM observation of clay particles in sediments was performed on freshly broken fragments of core
121 previously coated with a carbon film using a JEOL JSM IT500 scanning electron microscope equipped with
122 Secondary Electron (SE), Backscatter Electron (BSE) detectors and coupled with a Bruker linxeye Energy
123 Dispersive X-ray Spectrometer (EDX). The analytical conditions for quantitative EDX analysis of clay
124 minerals were as follows: acceleration voltage 15 kV, current beam 1 nA, counting time 60 s, working distance
125 11 mm, and analytical area of ~ 2 μm. The standards used for the EDX quantitative analysis consisted of albite
126 (Na, Al, Si), almandine (Mg, Fe), diopside (Ca), orthoclase (K) and spessartite (Mn). Matrix corrections were
127 performed using an integrated program called PhiRhoz correction. The reproducibility of the standard analyses
128 was 1.5% for all chemical elements, except Na, for which the reproducibility was 3%.

129 From north to south, five subzones (A to E) have been selected based on available data (seismic profiles,
130 multibeam bathymetry and CHIRP profiles) in order to perform a statistical analysis on the length and
131 orientation of polygon edges. The centre-to-centre distances between every pair of polygons were measured
132 and plotted on a polar diagram using a sheet of tracing film repeatedly placed with its centre over an object,
133 similar to the method of strain analysis (Ramsay, 1967). The relative positions of all surrounding objects are
134 plotted until a central vacancy field emerges, defining well-defined fabric ellipses. The method requires the
135 assumption of a statistically isotropic initial distribution of objects in which objects are unlikely to be closer
136 than a minimum distance apart. It means that fabric ellipses are due to anisotropic conditions during polygon
137 initiation, with a minor axis parallel the direction of the minimum horizontal stress.

Geological settings

139 The present-day crescent-shaped Grenada Basin (according to Mann, 1999 and Picard et al., 2006) results
140 from the latter 56-Ma geodynamical evolution of the Caribbean plate movement forming the Greater Arc of
141 the Caribbean (GAC) subduction zone (Ladd & Sheridan, 1987; Iturralde-Vinent & MacPhee, 1999;
142 Audemard et al., 2009; Pindell et al., 2012; Boschman et al., 2014; Münch et al., 2014; Legendre et al., 2018).
143 It is bounded to the west by the Aves Ridge, to the east by the Lesser Antilles Arc (LAA), to the south by the
144 shallow Venezuelan continental shelf and to the north by the Saba Bank (**Fig. 1**). Currently, the American
145 plates are subducting below the Caribbean plate at a mean rate of 2 cm/y (DeMets et al., 2000). The LAA
146 subduction zone marks the eastern boundary of the Caribbean Plate, whereas the Aves Ridge corresponds to
147 the southern part of the remnant GAC that was exposed between approximately 88 and 59 Ma (Fox et al.,
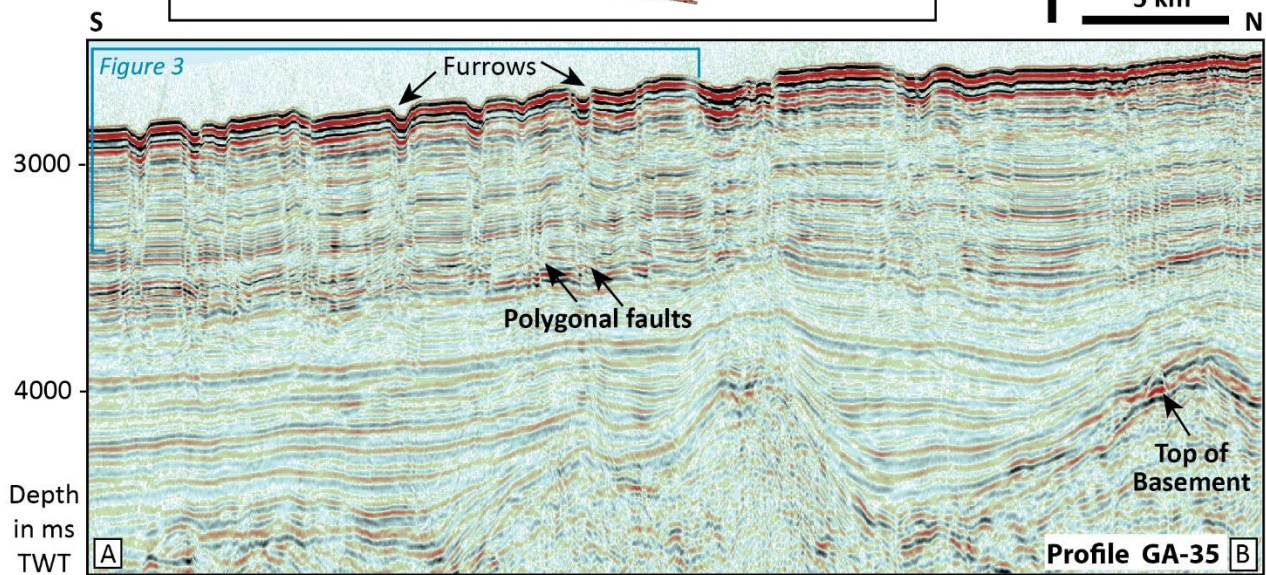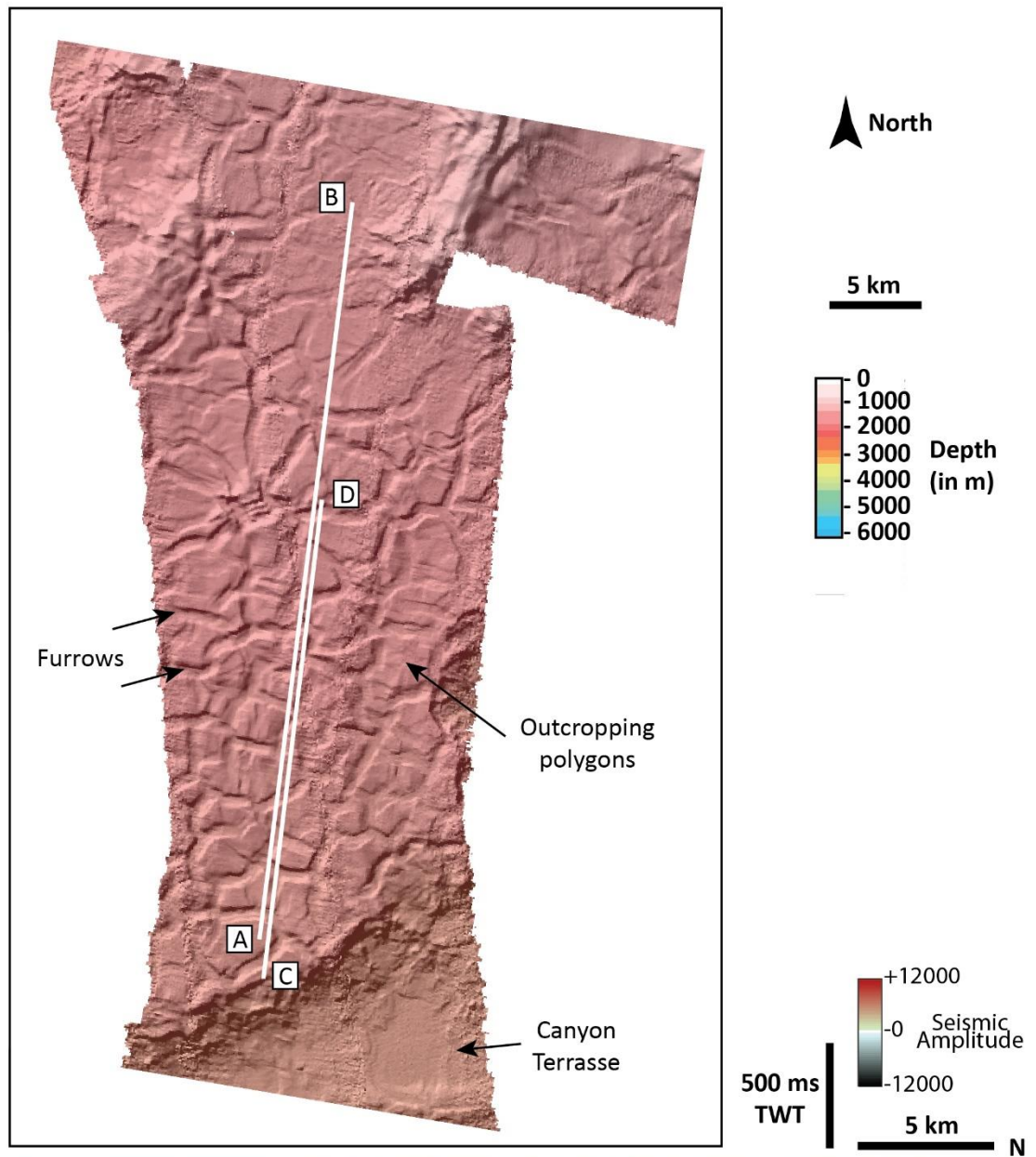
148   1971; Bouysse et al., 1985; Bouysse & Westercamp, 1990; Neill et al., 2011). The Grenada Basin has long
149   been considered a typical backarc basin between the Aves Ridge and the LAA. However, its morphology varies
150   from a rough ~1000-2000 m deep bathymetry and a Moho ~25 km deep in the North and a flat ~3100 m
151   bathymetry and a ~10-15 km deep Moho in the South (Gómez-García et al., 2019; Padron et al., 2021). This
152   is a marginal basin partly underlain by oceanic crust (Christeson et al., 2008; Allen et al., 2019; Padron et al.,
153   2021), adjacent to an oceanic island arc, that receives volcaniclastic debris from the bordering volcanic arc
154   and, to a lesser degree, the remnant arc (Carey & Sigurdsson, 1984; Parra et al., 1986; Murray et al. 2018).
155   However, previous sedimentological and geochemical studies have indicated that Grenada Basin sediments
156   are originated from two principal sources: volcanogenic material from the LAA, and terrigenous material
157   eroded from the South American continent (Pautrizel & Pons, 1981; Kinder et al., 1985; Bowles & Fleischer,
158   1985; Parra et al., 1986).

Seabed giant polygons and related polygonal faults

160   Seabed polygons are separated from the neighbouring polygons by 700-1500 m wide and 10-60 m deep
161   furrows (compared to the regional seafloor) with a flat bottom (**Fig. 2**). The polygons are ranging from 2000
162   to 3000 m on average. However, in the SGB the seabed polygons are much wider by a factor of 50-to-100%
163   where they can reach 5000 m in length, suggesting that the size of polygons depends on the location within
164   the basin.

165

166   **Figure 2**: Top: Shaded relief map of seafloor along the seismic profile GA-35 showing 2 to 3 km wide
167   polygons bounded by ~40 m deep furrows. Bottom: Seismic profile AB (GA-35 close-up view) displaying
168   polygonal faults affecting a ~1000 ms TWT thick interval. The polygonal faults are organized in set of small-
169   throw normal faults distributed beneath seafloor furrows. The furrows are the result of stacked depressions
170   down to ~300 ms TWT below seafloor.

171

North

5 km

Depth
(in m)

| 0 |
| 1000 |
| 2000 |
| 3000 |
| 4000 |
| 5000 |
| 6000 |

Furrows

Outcropping
polygons

Canyon
Terrasse

+12000
-0   Seismic
      Amplitude
-12000

500 ms
TWT

5 km

S

N

Figure 3

Furrows

3000

Polygonal faults

4000

Top of
Basement

Depth
in ms
TWT

A

Profile GA-35   B

172

On profile AB (GA-35 close-up view in sub-zone B), seafloor furrows are generally seen as small depressions affecting underlying horizons down to 200-300 ms TWT below seafloor (**Fig. 2**). The vertically stacked furrows are consistently located above small-scale faults affecting an interval ranging from 700 to 1200 ms TWT. The faults are characterized by various reflectors offsets, typically a few tens of ms TWT and they reach the seabed where they bound furrows. On high-resolution Chirp profiles, and despite a 20X vertical exaggeration, the polygons have very steep flanks (~3°), defining depressions (or furrows) that are 800-1500 m wide and 40 m deep compared to the 0,3° smooth regional slope (**Fig. 3**). Very high amplitude reflections occur right beneath the seabed creating large hyperbolae. A seismic profile displayed at the identical horizontal scale shows that each depression is bounded by faults reaching the seabed (**Fig. 3**). The polygonal faults are characterized on seismic profiles by an intense dimming of reflections on both edges of the fault planes suggesting that fluids are currently migrating upward.

Figure 3: Very high-resolution seismic profile (CHIRP) at the identical horizontal scale than the corresponding seismic profile GA-35. The furrows are affecting the present-day seafloor and they are ~1500 m wide and ~40 m deep. The seabed furrows represent the top of an underlying polygonal fault system (PFS). The bottom of furrows is characterized by very high amplitude reflections compared to well-bedded horizons between furrows.

Profile GA-35
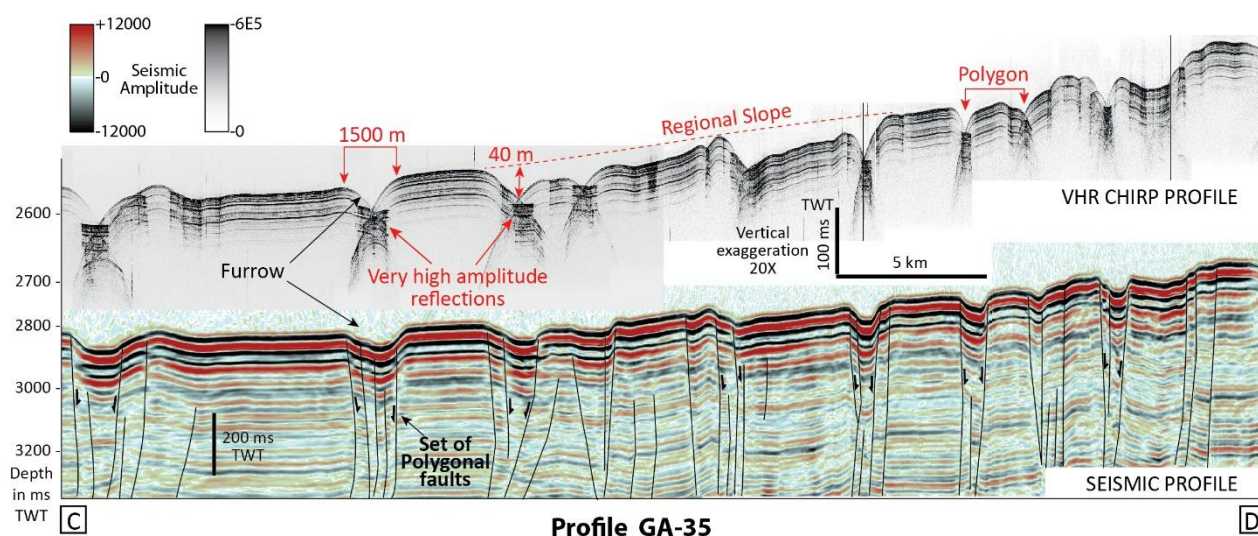
In more details all faults are normal and they are organised in set of 2-5 parallel faults (**Fig. 4**). Within the set of faults, the depressed reflections are vertically stacked and the offset along the fault plane is decreasing towards the seabed. At depth, the throw along a fault plane is progressively decreasing at the base of the polygonal fault interval where the lowest horizons do not appear affected (**Fig. 4**). The maximum throw along the fault planes has been identified at the transition between Early and Middle Pliocene (**Fig. 4**).

Figure 4: Detailed view of seismic profile GA-35 displaying decreasing offsets along fault planes both upward and downward from. The maximum throw is located at the transition between Early and Middle Pliocene all over the Grenada Basin. Units were correlated and described in Garrocq et al. (2021).
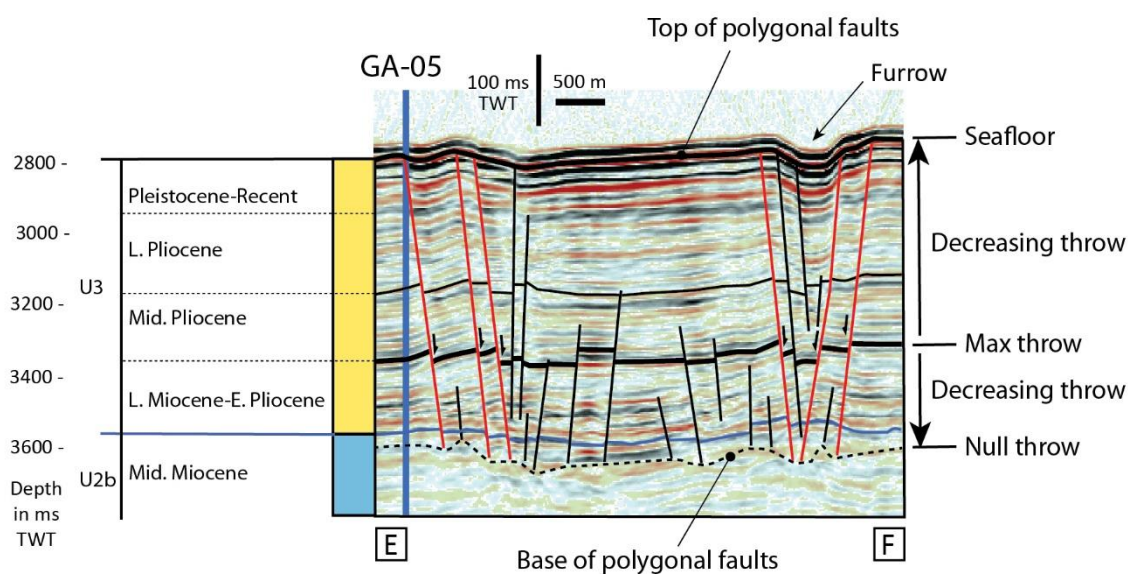

Nature of sediments

The present-day Antillean sediments are mainly of mafic-affinity, rich in pyroxenes and amphiboles but poor in quartz and biotite (in agreement with the andesitic composition of the volcanogenic material related to the LAA activity), whereas the South American supply is essentially of felsic-affinity, composed of quartz and phyllosilicate minerals, such as biotite, muscovite, and chlorite (Pautrizel & Pons, 1981). Clay mineralogy of two grab cores (GR-07 and GR-08) collected during the GARANTI cruise display very similar patterns. The bulk analysis shows a high clay content, mostly composed of smectite, illite/muscovite and kaolinite with subordinate chlorite and pyrophyllite, mixed with non-clay minerals such as pyroxenes, plagioclases, quartz and calcite (**Fig. 5**). The disappearance of chlorite and pyrophyllite X-ray reflections as well as the strong decrease in the peak intensity of illite/muscovite present in the XRD pattern of the fraction <2 µm indicate that these minerals are coarse grained and probably related to clastic metamorphic-derived source (**Fig. 5**). The XRD patterns of the fraction <2 µm are similar for both samples, with a very high smectite content and lower amounts of kaolinite and illite/muscovite. Based on cation exchange capacity measurement for the bulk material, the smectite content has been estimated to about 50% in both samples.

Figure 5: XRD analysis of grab cores GR-07 and GR-08. Top: bulk analysis displaying very similar patterns with a high clay content (smectite: sm, illite: Il, chlorite: ch and kaolinite: ka) and some other minerals (pyroxenes: py, plagioclases: pl, quartz: qz and calcite: ca). Bottom: analysis of the fraction <2 µm for both samples GR-07 (blue curves) and GR-08 (green curve) displaying very high smectite content, high kaolinite peaks and low illite peaks.
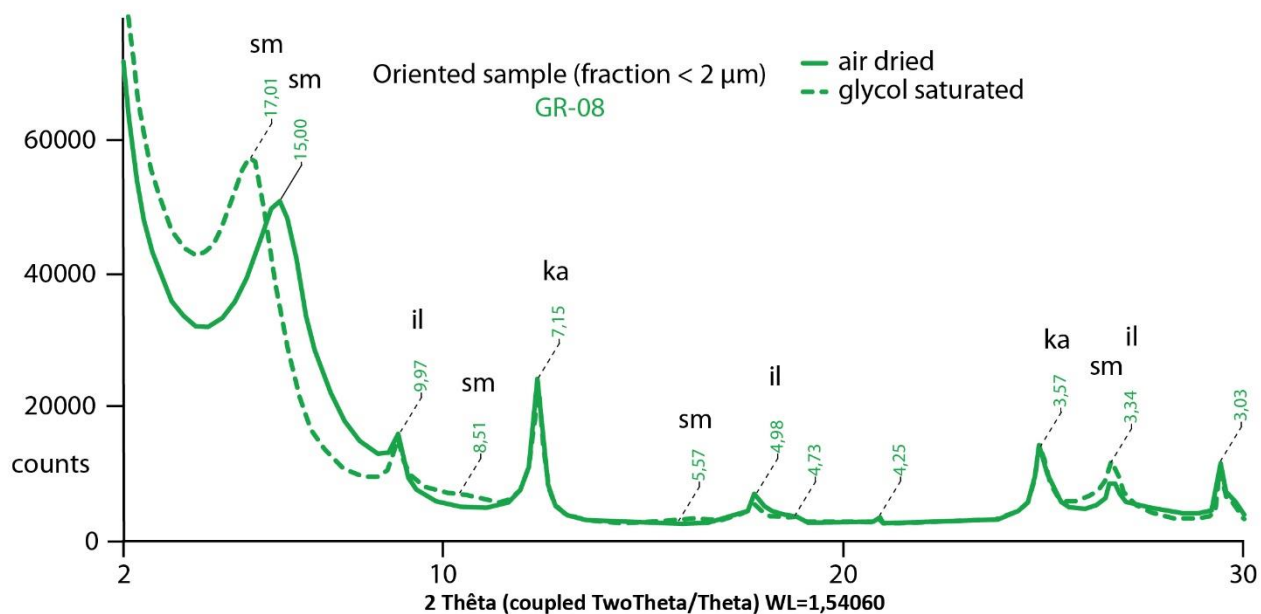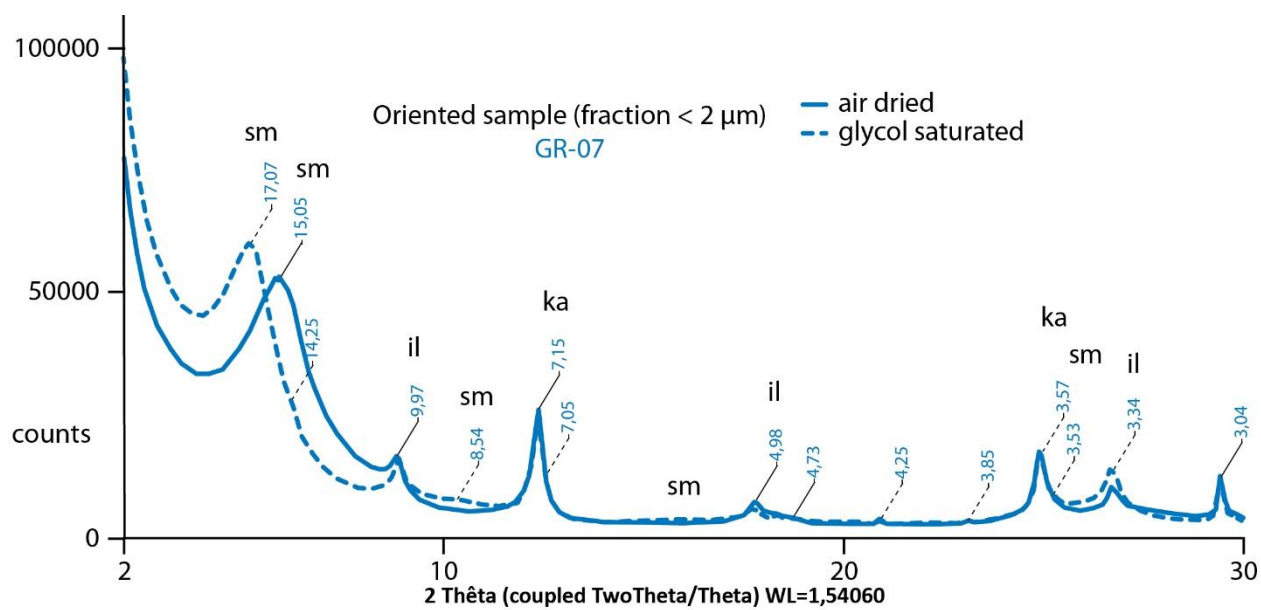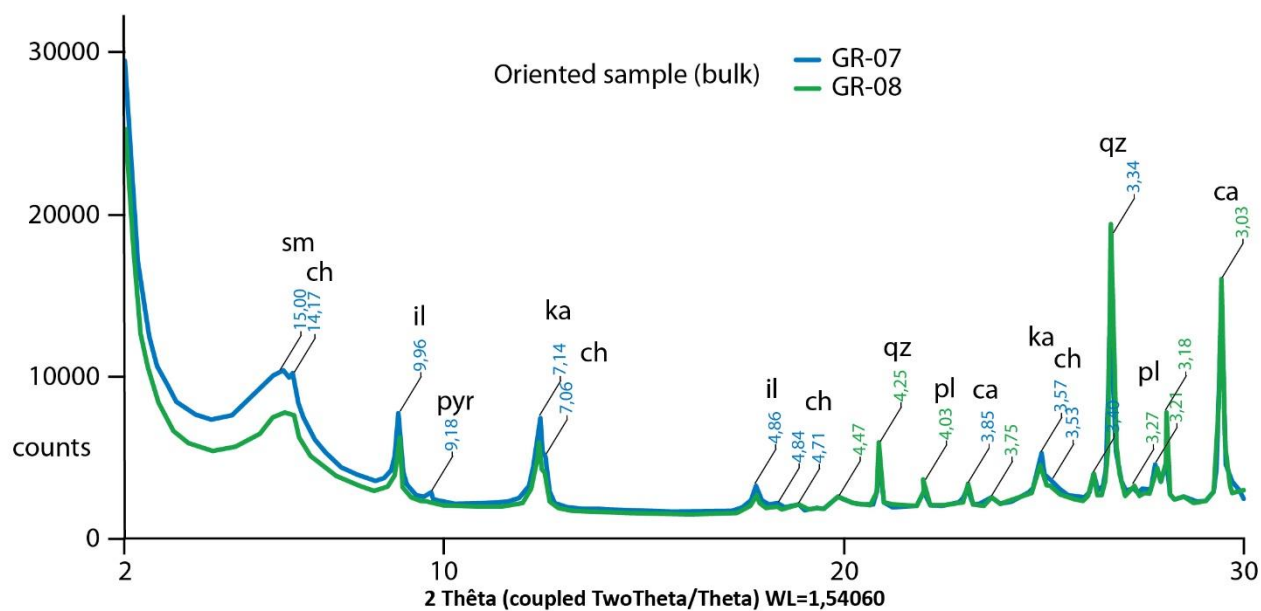
224　　　The SEM photographs shows that the sediments are dominated by smectite and kaolinite (**Fig. 6**). The

225　　calcite content is provided by the pelagic sedimentation of foraminifers although other minerals, such as

226　　feldspars (plagioclases), pyroxenes and quartz represent a minor contribution. The collected seabed sediments

227　　are primarily composed (>50%) of smectite at the grab cores location.

228　　　Chemical point analyses of the clay particles observed with SEM indicate that smectite is dioctahedral and

229　　is rich in Al and Fe with a layer charge mostly satisfied by K in interlayer position (**Fig. 6**). Such a chemical

230　　composition is similar to that of the potassic ferriferous beidellites characterized in the volcanogenic clay

231　　material in recent marine sediments (Desprairies and Bonnot-Courtois, 1980; Parra et al., 1985). In these

232　　sediments, smectite is generally derived from the diagenetic transformation of volcanogenic material

233　　(including volcanic ashes) into clay minerals. Conversely, kaolinite is usually derived from the weathering or

234　　the hydrothermal alteration of Al-bearing silicates in low pH environments and it is considered as a clastic

235　　material in marine sediments.

236

237　**Figure 6**: Top and bottom: SEM photographs of samples GR-07 (blue) and GR-08 (green). Both samples are

238　　dominated by smectite and kaolinite but smectite represents more than 50% of the bulk volume. The calcite

239　　peaks are derived from pelagic foraminifers; Middle left: Representative chemical analyses of smectites and

240　　the corresponding calculated structural formulae. Total iron was arbitrarily considered as Fe^{3+} ; Middle right:

241　　Al_2O_3-Fe_2O_3-MgO plots of the point chemical analyses of smectite particles from the two grab cores (GR-07

242　　and GR-08) collected during the GARANTI cruise.
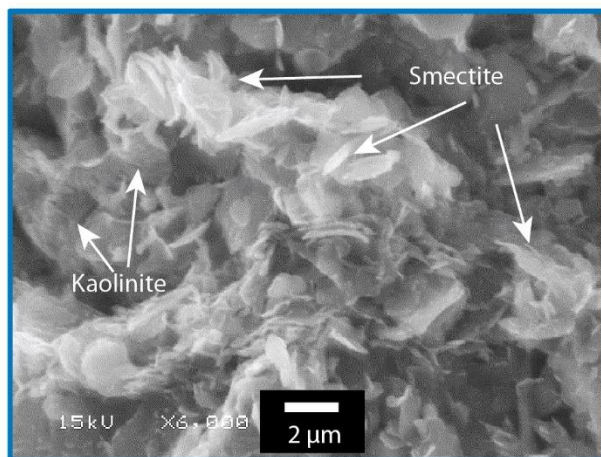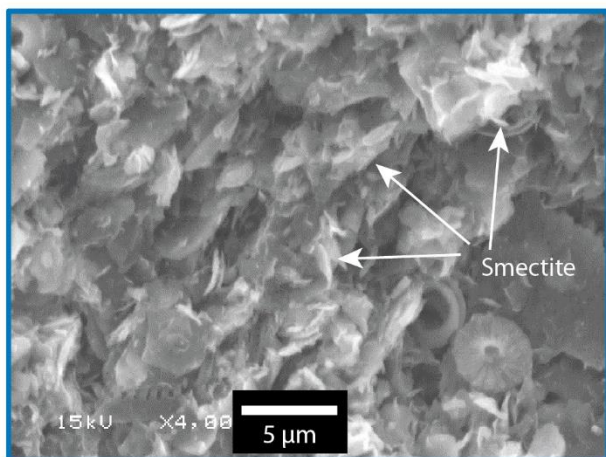
	GR-07	GR-08
SiO_2	48.57	46.36
Al_2O_3	19.65	19.84
Fe_2O_3	7.12	10.17
MgO	2.53	2.13
TiO_2	0.12	0.21
MnO	0	0
CaO	1.2	1.49
Na_2O	0.08	0.08
K_2O	3.13	3.16
Total	82.4	83.44
Number of cations (basis 11 oxygens)		
Si	3.63	3.48
Al^{IV}	0.37	0.52
Al^{VI}	1.36	1.24
Mg	0.28	0.24
Fe^{3+}	0.4	0.57
Ti	<0.01	0.01
Mn	0	0
∑oct	2.04	2.06
Na	0.01	0.01
Ca	0.1	0.12
K	0.3	0.3
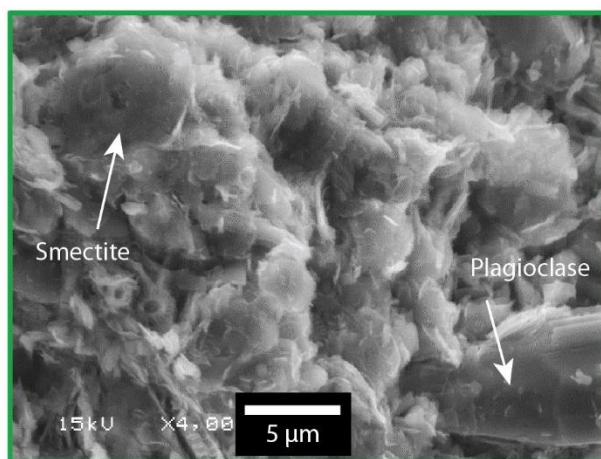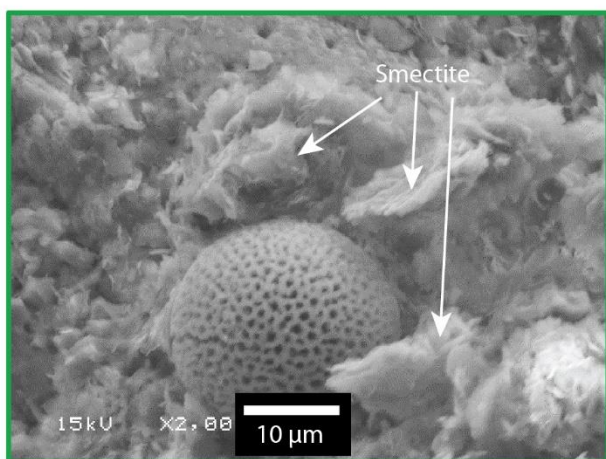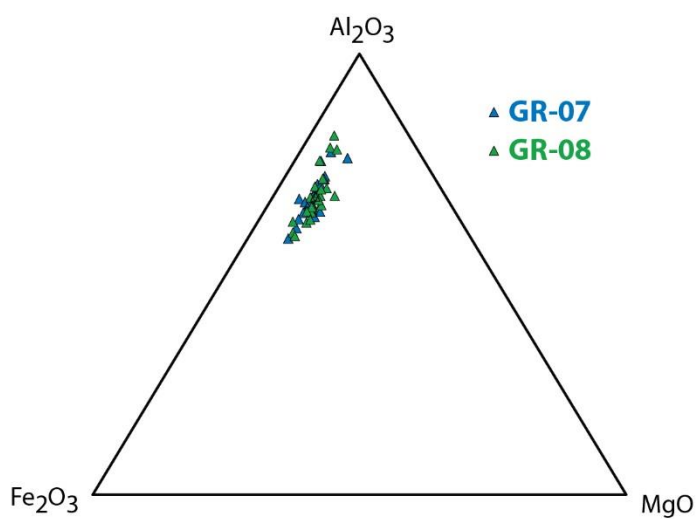
Seabed polygon organization

The polygons in the sub-zones A and B are very similar in size and shape (**Fig. 7**). However, they are 10-15 m deep in sub-zone A and 40 m deep in sub-zone B compared to the regional seafloor. They are characterized by 3 mains directions oriented N170-N10°, N30-50° and N90-110°, with lengths of 1260/1274, 1190/1208 and 1345/1374 ±15 m respectively. The basic shape is a polygon with a major axis of ~2400/2500 m in length in sub-zones A and B.

The sub-zone C is characterized by polygon edges oriented N170-10°, N30-50° and N70-90° with lengths of 1070, 1274 and 1047 ±15 m respectively. This defines polygons with a major axis of ~2250 m in length on average and 40-60 m deep bounding seafloor furrows.
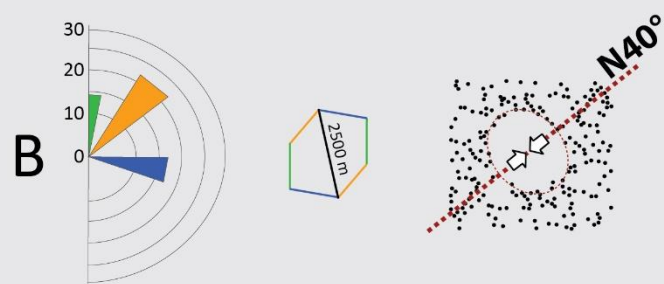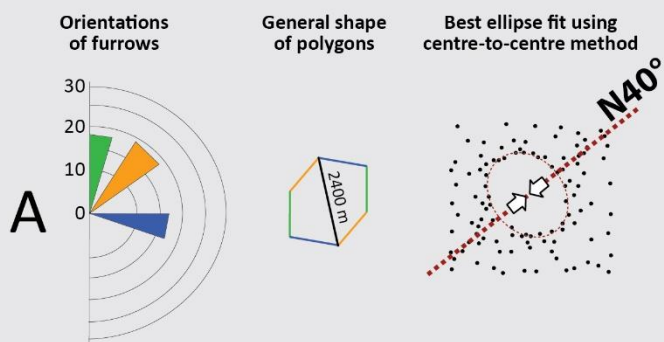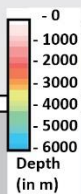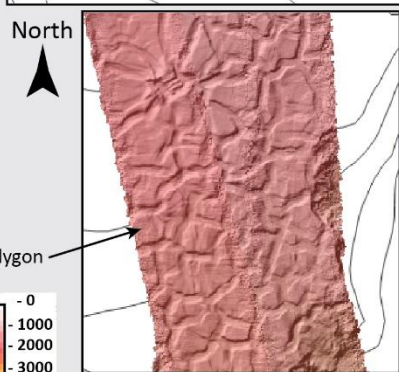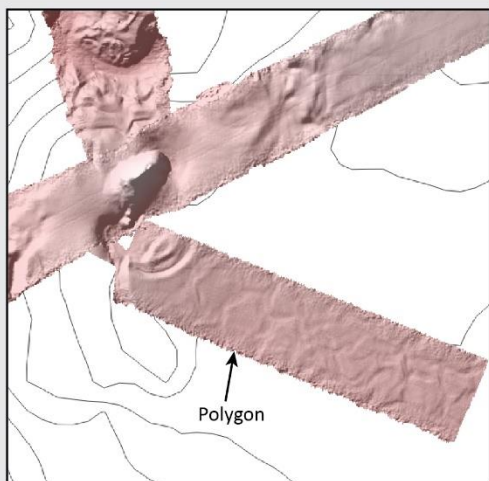
The sub-zone D is characterized by polygon edges oriented N10-30°, N30-50° and N70-90° with lengths of 1245 m ±15 m for every direction. They define elongated polygons with a major axis of ~3100 m in length on average and 30 m deep bounding seafloor furrows.

The sub-zone E displays polygon edges oriented N30-50°, N50-70° and N70-90° with lengths of 1653, 1935 and 1677 ±15 m respectively. They define very elongated polygons with a major axis of ~5000 m in length, clearly visible on the bathymetric map. The seafloor furrows are 20-30 m deep.
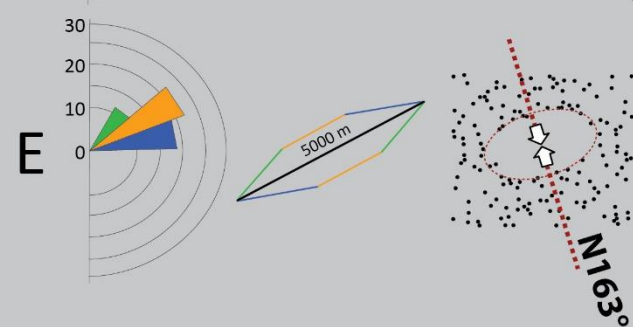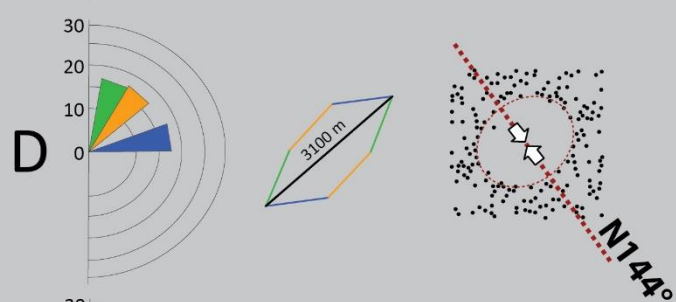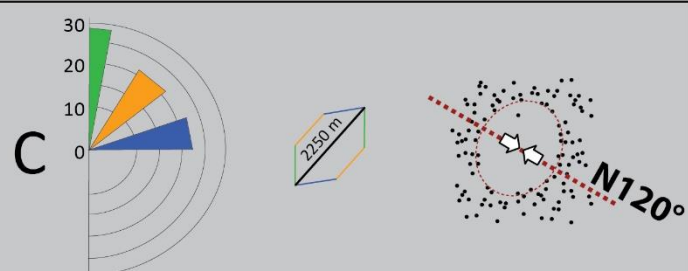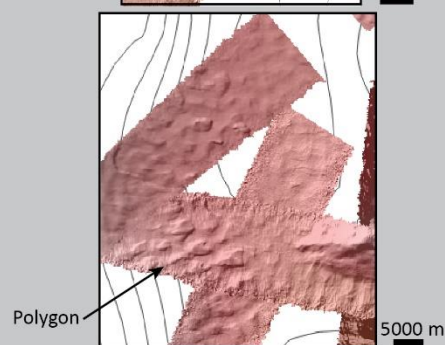
In the NGB the polygons are very similar in shape and orientation. The ellipses obtained from the centre-to-centre method show a minor axis oriented N40° indicating the main direction of anisotropic contraction of polygons. In the SGB the polygons are more elongated and their orientation progressively rotates southward. Seafloor furrows are deeper in the north than in the south by a factor of two. The minor axes are oriented N120°, N144° and N163° respectively, indicating that they are progressively changing towards the SGB. Consequently, two main areas are defined in the Grenada Basin in the north and the south by both the general shape of polygons and the direction of the minor axis obtained from the centre-to-centre method.

Figure 7: Statistical analysis conducted on seafloor polygons bounded by furrows in sub-zones A to E. Polygons are very similar in size and shape in sub-zones A and B in the NGB, although they are getting longer from sub-zone C to E towards the SGB. This is confirmed by best fit ellipses obtained from the centre-to-centre method, giving a minor axis oriented N40° in sub-zones A and B whereas it is turning from N120° in sub-zone C to N144° in sub-zone D and N163° in sub-zone E.

North Grenada Basin

South Grenada Basin

North

Depth (in m): 0, -1000, -2000, -3000, -4000, -5000, -6000

Orientations of furrows

General shape of polygons

Best ellipse fit using centre-to-centre method

A — 2400 m — N40°
B — 2500 m — N40°
C — 2250 m — N120°
D — 3100 m — N144°
E — 5000 m — N163°

Polygon

2000 m, 3000 m, 5000 m
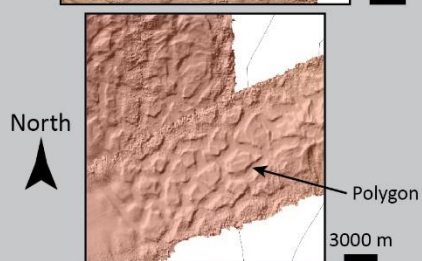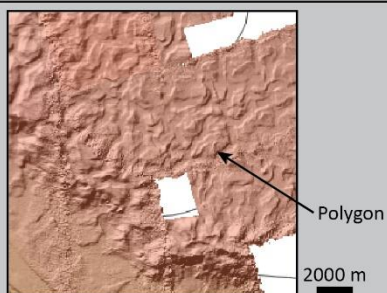
Discussion

Origin of sediments and sequences

The volcanic arc is volumetrically the most important source for sediments, with abundant volcaniclastics being produced by explosive subaerial and/or subaqueous eruptions and secondary erosion of the arc complex (Carey & Sigurdsson, 1984). Except for direct ash-fall deposits, the recent sediments in the flanks of the Grenada Basin are composed of volcanogenic debris emplaced by turbidity currents and debris-flows coming from both the LAA (Carey & Sigurdsson, 1978; 1980; Sigurdsson et al., 1980; Deplus et al., 2001; Brunet et al., 2016; Le Friant et al., 2020; Seibert et al., 2020) and from the Aves Ridge (Bader et al., 1970; Holcombe et al., 1990). The hemipelagic sedimentation mixing dispersed ash and clastic clays coming from South America is the dominant process in the deeper part of the Grenada Basin (Sen Gupta et al., 1982), entering the Grenada basin by northward flowing Caribbean ocean currents (Corredor et al., 2004).

This mixed sedimentation is active since middle Miocene (Aitken et al., 2011) defining unit U3 (**Fig. 8**) identified on seismic sections as chaotic and semi-continuous tabular high amplitude reflectors (Garrocq et al., 2021). The LAA is composed of mostly andesitic igneous rocks (MacDonald et al., 2000) whose weathering products carry a distinctive signature. Smectites and kaolinite are the dominant clay minerals produced by the weathering of Lesser Antillean igneous rocks, with over twice as much smectite produced as kaolinite. Another typical weathering characteristic of an igneous island arc terrane is the absence of illite or illite-smectite mixed layers. Hydrothermal illite and illite-smectite mixed-layers may form in the geothermal fields related to the volcanic activity, as documented on the islands of Guadeloupe to Grenada (Parra et al., 1986; Mas et al, 2003; Mas et al. 2006; Murray et al., 2018). However, the spatial extension of the geothermal areas is too limited to exert a significant contribution to the clay material accumulated in marine sediments. Hence, high smectite and low illite contents are typical of sediments with a volcanogenic (Lesser Antillean) source (Pautrizel & Pons, 1981; Parra et al., 1986). Crustal terranes of the South American continent made of granites and gneisses act as the source area for non-volcanic abiogenic sediments deposited in the Caribbean. Tropical weathering of these continental rocks produces four dominant clay minerals: illite, kaolinite, smectites, and chlorite. This fine-grained terrigenous material is carried in suspension to the southeast Caribbean by major rivers, particularly the Amazon and the Orinoco (Bowles & Fleischer, 1985). Thus, a clay mineral assemblage characterized by high abundances of illite, kaolinite, chlorite and minor pyrophyllite is typical of a South American terrigenous source, as is the presence of detrital quartz (Pautrizel & Pons, 1981). Some deep channels across the Aves Ridge permitted the transport of the Venezuela Basin bottom water (commonly labeled Caribbean Bottom Water or CBW) into the Grenada Basin (Kinder et al., 1985).

Unit U2 (Early to Middle Miocene) was fed by the Orinoco whereas its delta front was oriented North-South towards the Grenada basin. During Tertiary times the Orinoco drainage basin and its associated delta has migrated eastward over more than 500 km because of the eastward deformation in north Venezuela due to the Caribbean plate/South America relative movements (Beck et al., 1990; Pindell, 2006, Audemard et al., 2009). Presently, the turbidite system issued from the present-day Orinoco delta develops at the eastern edge of the East Caribbean active margin partly above the large southern part of the Barbados accretionary prism

and downslope at the front of this prism, within the Demerara abyssal plain (Deville et al., 2015). Unit U2 is

marked by a shallowing of the facies corresponding to a progressive infilling of the Grenada Basin (Garrocq

et al., 2021). Sediments in Unit U1 are deep-water, pelagic and volcanogenic shale and siltstone, with some

biogenic limestone in the deeper parts (Ysaccis, 1997), whereas seismic reflections in Unit U0 are very chaotic

but they are well organized in some places, possibly related to cretaceous sediments.

Figure 8: Top: Seismic profile GA-05 and its line-drawing displaying the PFI in the NGB. The polygonal

faults do not develop where deep turbiditic channels are present. The PFI is getting thicker southward affecting

almost all unit U2. Units U0 to U3 were correlated on GARANTI seismic data from previous studies and

ODP/DSDP wells (Garrocq et al., 2021); Bottom: Seismic profile GA-29 and its line-drawing displaying the

PFI in the SGB. In both the western part of the SGB and the Aves Ridge, the polygonal faults are reaching the

seafloor. The base of the PFI varies from west to east generally affecting the top of U2. In the eastern part of

the SGB the PFI is thinning eastward (both the top and the base of the PFI are crosscutting stratigraphic

horizons) and abruptly ends 40-70 km off the volcanic arc.

326
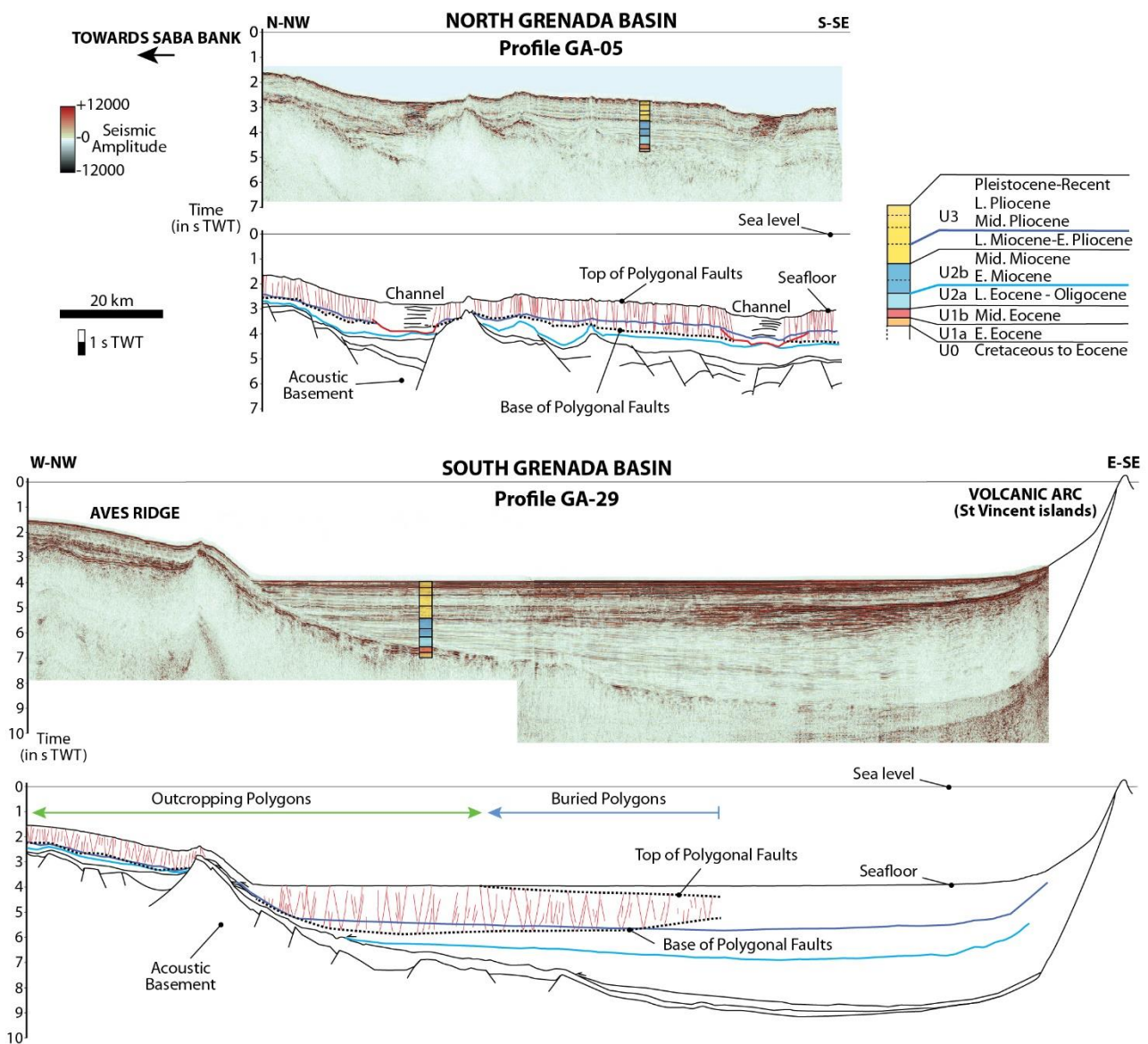
In the NGB, the polygonal faults reach the seafloor, except in the vicinity of deep turbiditic channels where they do not develop at all (**Fig. 8**). The PFI is getting progressively thicker southward as its base is getting deeper. However, the PFI abruptly ends at the toe of the Saba Bank (not shown in this study but visible on profile GA-15C in Cornée et al., 2021).

In the western part of the SGB, the PFS are affecting unit U3 (**Fig. 8**) and giant polygons are cropping out at the seabed. The base of PFI is not concordant with the base of unit U3 and, as shown on **Fig. 4**, it is undulating over the Grenada Basin within the top of unit U2, depending on the depth at which the faults have propagated downward. In the centre of the SGB the PFS do not reach the seafloor nor unit U2 where the PFI appears buried (500 ms TWT below seafloor) and thinner (700 ms TWT) defining a lenticular shape. The PFS abruptly end eastward at a distance of ~40-70 km from the LAA. On the Aves ridge, the PFI appears thinner by a factor of 2, which is correlated with thinner sedimentary sequences.

The total area covered by both outcropping and buried polygonal faults is about 75000 km² (55000 + 20000 km² respectively), defining a crescent shape more or less concordant with the shape of the Grenada Basin (**Fig 1**).

Polygonal faults orientations as a marker of basin extension

The main hypothesis for polygonal faults formation considers a finite bed length extension and the development of conjugate fault planes with extensional offsets (apparent normal faults) due to a bulk volume loss of pore fluids. This process leads to a thinned sequence, which is partly compacted (Cartwright & Lonergan, 1996; Gay et al., 2004). The consequences are that the complex polygonal fault systems in mudstone dominated sequences formed due to volumetric contraction and concomitant fluid expulsion (Shin et al., 2008; Gay et al., 2004; Gay et al., 2007) that leads to shrinkage in mud-dominated sequences (Cartwright & Lonergan 1996; Dewhurst et al. 1999). Normal faulting related to burial and sediment loading is not a common process that has been already proposed for rocks deformation, probably because soft sediments like clays have a specific rheological behaviour. The dominant orientation of minor axis of fabric ellipses obtained from the centre-to-centre method as well as their bending in the slope direction suggests the interaction of gravity-driven shearing of the compacting interval. For example, sedimentary structures, such as dewatering pipes and sand volcanoes (Waldron, 1988), may display diffuse outlines but nonetheless show anticlustered distributions. A radial stress tension related to the volumetric contraction of clay could allow to reduce the lithostatic mean stress, also increasing the differential stress, and then to reach shear failure along a Coulomb-type conventional envelope. However, this process assumes that 1) the faulted material has a common frictional envelope, 2) the lithostatic stress state prior to faulting due to compaction was sub-critical (i.e. close to shear failure), and/or 3) the stress tension related to the volumetric change is large enough. In such unlithified and uncompacted clay sediments, the coefficient of Earth pressure at rest (Ko) is generally large (0.45–0.8) implying a little differential stress due to the vertical loading (Earl, 1997; James, 2006). This suggests that a high horizontal tension due to internal contraction is needed to get the failure envelope (Cartwright & Lonergan, 1996), coupled to an external regional extension (Laurent et al., 2012; Bureau et al., 2013). This model suggests that

progressive sediment loading acts as a centrepiece in the initiation and propagation of polygonal faults (Gay et al., 2004; Gay et al., 2007; Reiche et al., 2011). It also implies that, at great burial depths, the compaction through the process of volumetric contraction ends and the dissolution–precipitation mechanisms become dominant (Gay et al., 2004). Clausen et al. (1999) have suggested that PF developed within a broadly polygonal array due to gravitational sliding influenced by far-field tectonic stresses, even if Wrona et al. (2017) have recently suggested that such processes played no or an imperceptible role in the growth of this specific North Sea system. However, the hypothesis that layer-parallel displacements of these faults are accommodated by regional extension of the host strata has been confirmed in various basins, such as in the Lower Congo Basin (Gay et al., 2004) or in the Angola basin (Ho et al., 2018), and more recently by field studies showing that a radial extension may account for PFS development (Antonellini & Mollema, 2015; Petracchini et al., 2015). Syn-thrusting non-diagenetic polygonal normal faults were reported in the Cingoli anticline. The PF nucleated into multi-directional stretching processes that are consistent with the fault slip indicators (Petracchini et al., 2015). This study also reported that faults are not systematically parallel to the general trending anticline axis suggesting an evolving pattern of PFS influenced by structural paleo-stresses conditions. So, the development of PFS at the seabed could thus be indicative of the present-day strain state within the sedimentary column (Tuckwell et al., 2003; Ho et al., 2018; Jitmahantakul et al., 2020).

In the NGB, the strain ellipses show a similar minor axis orientation of N40° in both areas A and B, meaning that all polygons are contracting following the same major direction. It is now commonly admitted that such direction of contraction is parallel to the minimum principal stress σ3 (Petracchini et al., 2015; Ho et al., 2018), which represent a direction of extension within the sedimentary column. So, we assume here that the PFI is currently in extension following one major direction of N40°. The forearc-backarc domain has undergone a regional subsidence and a NE-SW extension since Late Miocene, evidenced in the Northern Lesser Antilles forearc (Boucard et al., 2021) and in the intra-arc Kalinago Basin (Cornée et al., 2021). The N40° extension evidenced from PF orientations thus may indicate that the upper sedimentary cover (unit U3 at least) is submitted to similar processes in the backarc. During this period, uplifts phases were moderate compared to this subsidence, which has submerged islands and previously uplifted areas (Bouysse, 1988; Mann et al., 1995; Feuillet et al., 2010; Philippon et al., 2020a; Legendre et al., 2018; Cornée et al., 2020; Cornée et al., 2021). The extensive deformation has triggered deeply-rooting NW-SE faults in the forearc (Boucard et al., 2021) and in the Kalinago Basin (Cornée et al., 2021). This is possibly explained by thermal relaxation related to the cessation of arc activity in the northeastern LAA (MacPhee et al., 1989; Jany et al., 1990; Philippon et al., 2020b) and/or by distal tectonics influence of subduction dynamics (Boucard et al., 2021). The more recent and continuous subsidence since Late Miocene - Early Pliocene may explain shallower depths of both the present-day seafloor and the base of unit U3, with an average depth of 2 s TWT (**Fig. 9**). The isopach map of unit U3 shows a constant thickness of about 0.7-0.8 s TWT, even in the area of Saba Bank, indicating a homogeneous subsidence in the entire area (**Fig. 9**).

In the SGB, the ellipses show a change in direction of the minor axis, indicating varying orientations of the extension of the PFI pointing towards the centre of the SGB where the curved depocenter of unit U3 follows

the curvature of the modern volcanic arc (**Fig. 9**). The major faults identified in the SGB (Speed & Westbrook, 1984; Pindell & Barrett, 1990; Pindell & Kennan, 2009; Aitken et al., 2011; Garrocq et al., 2021) do not seem to control the orientation of PF, indicating that the upper part of the sedimentary column, particularly unit U3, is actually in extension following a general subsidence in the south. In this area, the subsidence has significantly increased from Late Miocene to present, possibly explained by a southeastward regional tilting and/or a greater sediment compaction in response to sediment loading in the basin (Garrocq et al., 2021). The base of unit U3 is characterized by a sharp change in average depth from 2 to 5 s TWT west off Dominica island and a slight deepening to the South where it reaches about 6 s TWT west off Grenada island (**Fig. 9**). However, the isopach map of unit U3 shows a curved NE-SW depocenter with a maximum thickness of 2,3 km in the southwest indicating a higher subsidence rate in the south.

Figure 9: Left: isochron map of the base of U3 displaying a crescent shape following the LAA. There is a sharp change west off Dominica where U3 is strongly deepening of ~3 s TWT. From Dominica to the south of Grenada Island the base of U3 is slightly deepening to reach ~5,5 s TWT. U3 is very shallow on Saba Bank and on top of the Aves Ridge. Right: Isopach map of U3 showing a homogeneous thickness in the NGB. In the SGB, U3 progressively thickens southward, indicating a differential subsidence between north and south.
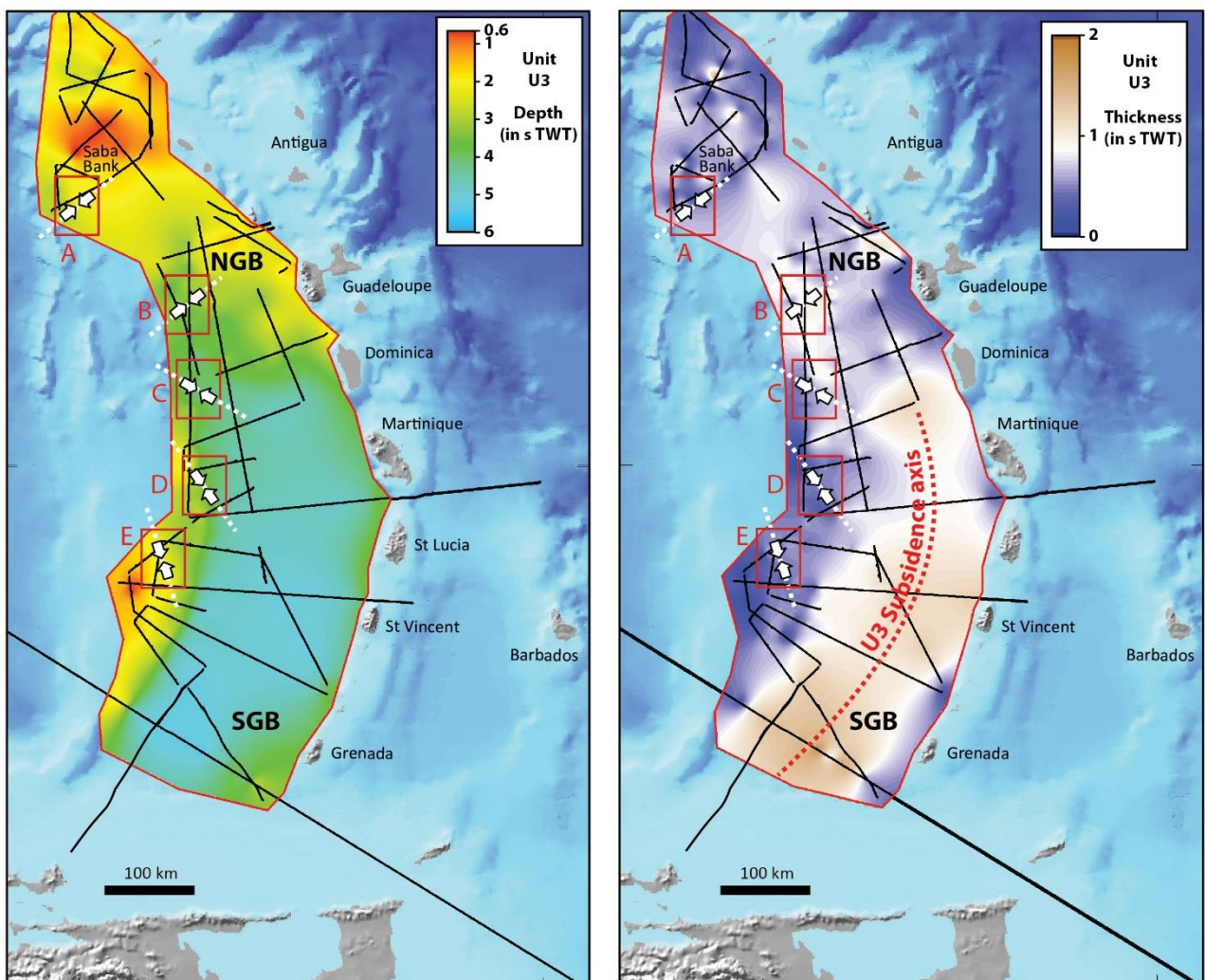
Factors controlling the initiation and propagation of polygonal faults

418   Lithological analyses conducted on wells penetrating polygonal fault intervals show that the amount of

419   shrinkage in layers appears to increase as the grain size decreases and smectite content increases (Dewhurst et

420   al., 1999; Gay et al., 2007). This composition forms a fine texture of flocculated particles, 2 μm in size,

421   submitted to shrinkage upon drying leaving voids that are about 5 μm in width (Forsberg & Locat, 2005). This

422   process occurs at a microscale, and could explain 1) the spontaneous contraction of mud-dominated sediments,

423   leading to the formation of normal faults at a wider scale and 2) the development of polygonal faults

424   outcropping at the seabed, meaning that the volumetric contraction can form during early compaction, leading

425   to a rapid bulk volume loss.

426

427   **Figure 10**: Schematic sketch illustrating the initiation and propagation of PF starting at the seabed. The PFS

428   started at the transition between Early and Middle Pliocene. They are then propagating both upward and

429   downward during sedimentation and as long as the sediment composition remains clay- and smectite-rich and

430   the extension is large enough to allow proper contraction of sediments.

431
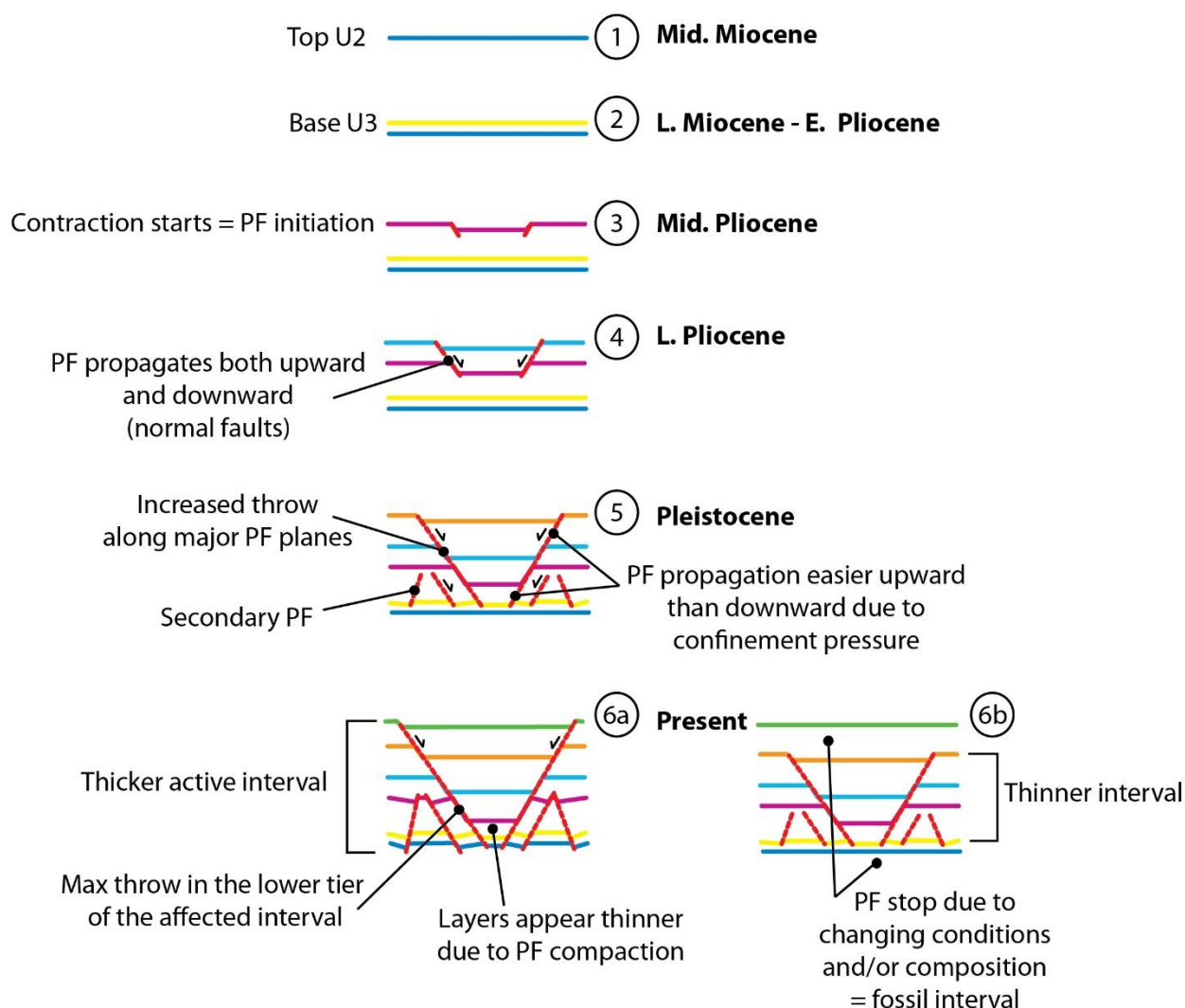
The PF initiation and propagation in the Grenada Basin can be summarized in an evolutionary model taking into account their morphology both at the seabed and on seismic profiles (**Fig. 10**). Unit U2 was fed by clastic metamorphic material coming from the Orinoco delta while it was oriented NS, which is not compatible with spontaneous volumetric sediment contraction at seabed (stage 1). During Late Miocene the lateral shift of the Orinoco river on the eastern flank of the LAA has limited the coarser metamorphic material input into the Grenada basin (Diaz de Gamero, 1996; Escalona & Mann, 2010). The base of unit U3 was more and more fed by smectite-rich sediments derived from the volcanic arc and/or coming from the South American continent through the CBW current (stage 2) and the contraction started during the Middle Pliocene (stage 3). The process of contraction has gone on as long as sediments deposited at the seabed had the composition required for PF development (Gay et al., 2007; Jackson et al., 2014). Increased dewatering during burial implied more displacement along faults (Jitmahantakul et al., 2020), which would continue to grow as long as the dewatering cell contracted volumetrically (stage 4). The PF propagated both upward and downward although the progressive reduction in bed length through contraction was balanced by an incremental increase in the amount of displacement distributed along the faults (stage 5). Fault propagation is much easier towards the seabed than at depth due to the confinement pressure, and the throw maximum along major PF planes is always found in the lower tier of the affected interval. At depth, secondary faults are initiated due to sediment loading in order to better drain the centre of polygons (stage 5). They display lower amount of displacement than the major polygonal faults at the same stratigraphic level, confirming that the nucleation of PF occurred where/when the throw is maximum (i.e. Middle Pliocene) (stage 6a). The kinematic model of polygonal fault growth in which the propagation of faults is discontinuous during basin infilling leads to a 4D interpretation of the whole polygonal faut system. In the eastern part of the SGB, the polygonal fault interval appears buried and the PFI is thinning towards the east, cross-cutting stratigraphic horizons. The eastern part of the Grenada Basin can be considered as a fossil interval of PF (stage 6b), whereas polygonal faulting remains active to the west and although the initiation point is at the same stratigraphic level both in east and west. This could reflect 1) a progressive westward migration of the extension domain affecting the upper part of the sedimentary column or 2) the western area remains dominated by clay- and smectite-rich sedimentation, whereas the eastern area has received different lithologies. Flank collapse events have occurred all along the LAA, resulting in debris avalanches, some of them involving large volumes of material (Deplus et al., 2001, Brunet et al., 2016). A striking characteristic of the deposits in the Grenada Basin is the presence of a thick chaotic unit in seismic data, about 250 ms TWT in thickness, west off emerged islands in the deep basin. Some of the debris avalanches have evolved into debris flows and turbidity currents, feeding the eastern deep basin with coarser material (Deplus et al., 2001). At this point, the change in sediment input (and composition) seems the most probable cause for stopping PF propagation in the east Grenada Basin.

Model of polygonal faults in the asymmetric basin of Grenada

Major differences in depths, morphologies and PF between the NGB and the SGB are evidenced along a NS profile (GH) (**Fig. 11**):

468 > The basin infilling is controlled by the available space for sedimentation. Due to repeated episodes of
469 uplift and emersion in the north, the thickness of the sedimentary cover is relatively thin with a maximum of
470 about 3 s TWT south of Saba Bank and west of Antigua. Unit U3 appears isopachous with a seabed slightly
471 deepening to the south, indicating that the present-day subsidence is homogeneous in the area. The continuous
472 subsidence in the south since Eocene has led to a very thick sedimentary cover of about 6 s TWT between the
473 Aves Ridge and the Grenada Island. Unit U3 is thickening southward with a relative flat seabed, indicating an
474 actual differential subsidence which is stronger in the south.

475 > Classical normal faults usually propagate parallel to the principal stress σ1, while hydraulic fractures
476 open in parallel to the intermediate horizontal stress σ2 and against the minimum principal stress σ3 (Cosgrove,
477 1995). However, PFS do not follow such behavior due to the anisotropy of unlithified cohesive fine-grained
478 sediments and the anisotropic stress attributed to perturbations of the regional stress field can control the PF
479 orientations (Ho et al., 2018). Volumetric contraction is a spontaneous process forming polygons by joints
480 growing from an initiation point in all directions at the same time, such as in cooling lava flows (Aydin &
481 DeGraff, 1988). In sedimentary basins, σ1 is generally vertical and corresponds to the lithostatic vertical stress
482 (σv) and we assume here that σ2 and σ3 are respectively perpendicular and parallel to the minor axis of fabric
483 ellipses obtained from the centre-to-centre method. In the north, the PFI abruptly ends at the toe of Saba Bank,
484 a lithified reefal and red algal platform (Cornée et al., 2021) in which PF cannot develop. PF are controlled by
485 a general N40° extension of the present-day backarc basin. In the south, PF are following the deepest point of
486 subsidence actually towards the south. The active interval of PF has continued growing until the present day
487 in the centre and in the west of the Grenada Basin whereas it has stopped or never developed in the east due to
488 coarser and/or less smectite-rich input coming from the active LAA.

489 > Between the NGB and the SGB, the change in depths, morphologies and polygonal faults orientations is
490 sharp, suggesting that both basins are presently submitted to very different tectonic regimes. The boundary
491 between both PF domains is estimated to be west off Dominica island, which is consistent with a NGB
492 underlain by about 90 Ma subducted lithosphere, whereas the subducted lithosphere is up to 120 Ma old
493 beneath the SGB (Müller et al., 2019). This is confirmed by a basement that remains high in the north, reaching
494 a maximum of about 4 s TWT in depth, although it is strongly deepening in the south, reaching a maximum of
495 10 s TWT. This limit between two underlying geodynamic domains may actually be recorded by shallow PFI
496 in the backarc domain.

497

498 **Figure 11**: Model of PF occurrence in the Grenada Basin. Between north and south the change in depths,
499 morphologies and polygonal faults orientations is sharp, suggesting that both basins are actually submitted to
500 very different tectonic regimes. The best fit ellipses extracted from the centre-to-centre method allowed the
501 identification of preferential contraction orientations in unit U3. It is assumed that the minor axis of the ellipse
502 represents the main orientation of volumetric contraction of sediments and it can be related to the minimum
503 principal stress σ3. σ1 and σ2 orientations are deduced from the orientation of σ3. The extension is N40° and
504 remains constant in the NGB, although it is changing (N120° to N144° to N163°) in the SGB, following the

U3 depocenter. Giant seabed polygons in the Grenada Basin and the underlying PFS are markers of the present-day (or recent) strain state within the upper sedimentary column.
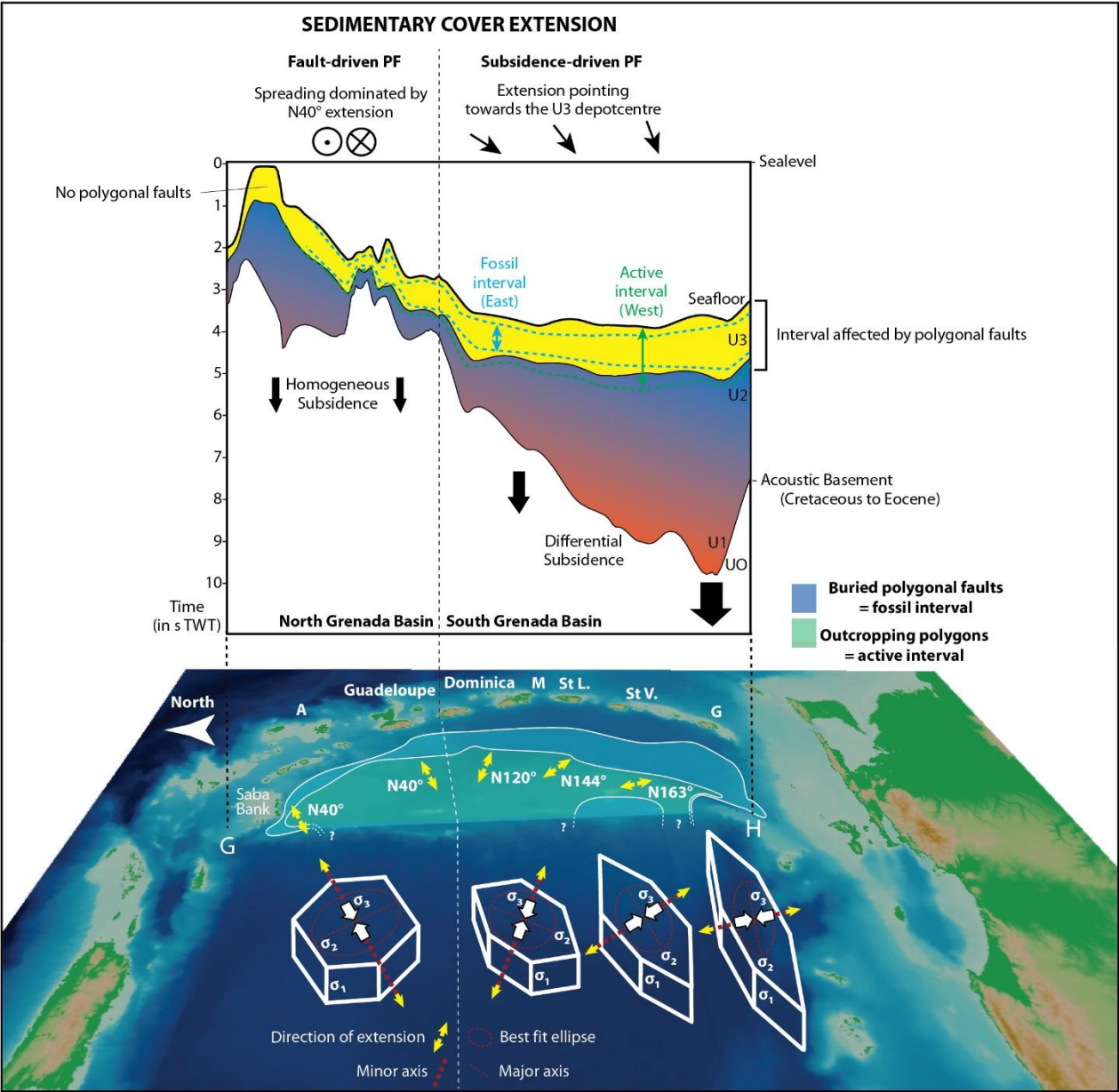
Conclusion

A regional acquisition of seismic data and multibeam imagery at a basin scale provided new insights on the recent Grenada Basin history and improved the understanding of post-depositional processes occurring in PFI. We have identified giant seabed polygons covering the widest area ever found on Earth, with a surface of approximately 55000 km², and even up to 75000 km^2 taking into account those which do not reach the seafloor in the centre and the eastern Grenada Basin. Moreover, the western extent of the PFS area is limited by our investigation area but we suspect that most of the Aves Ridge and even its western flank is concerned.

The horizon depths, seabed and thickness morphologies are very different in the NGB and the SGB, which is consistent with their respective and very different geodynamic histories. The NGB underwent repeated

episodes of uplift (including aerial exposures at some places) and subsidence although the SGB is on a continuous state of subsidence since Eocene. They are both subsiding since middle Pliocene but at different rates.

Surprisingly, different orientations of polygons have been evidenced in both domains. The polygons are very regular in the north, whereas they are more elongated in the south. The centre-to-centre method applied to seabed polygons provided major orientations of extension needed for polygons to initiate. In the NGB minor axes are oriented N40°, indicating a general NE-SW extension of the upper part of the sedimentary cover. This could indicate that the backarc basin is currently submitted to similar processes than the forearc. In the SGB, minor axes are progressively turning towards the south, pointing out the actual maximum subsidence point.

In both cases, these observations imply that the development of PFS at the seabed could thus be indicative of the present-day strain state within the upper sedimentary column. Further investigations, including extensive seismic acquisitions and sampling, must be considered in order to completely map the extent of both active and fossil/buried intervals in the entire Aves Ridge area as PFI could be a marker of both actual or passed strain states within affected intervals, which is of high interest for the characterization of tectonic contexts.

References

Aitken, T., Mann, P., Escalona, A., & Christeson, G. L. (2011). Evolution of the Grenada and Tobago basins and implications for arc migration. Marine and Petroleum Geology, 28(1), 235–258

Allen, R. W., Collier, J.S., Stewart, A. G., Henstock, T., Goes, S., & Rietbrock, A., and the VoiLA Team (2019). The role of arc migration in the development of the Lesser Antilles: A new tectonic model for the Cenozoic evolution of the eastern Caribbean. Geology, 47(9), 891–895. doi: https://doi.org/10.1130/G46708.1

Antonellini, M., & Mollema, P. N. (2015). Polygonal deformation bands. Journal of Structural Geology, 81, 45-58

Audemard, F. A., Keith J. H., Lorente, M. A., & Pindell, J. L. (2009). Key issues on the post-Mesozoic southern Caribbean Plate boundary. Geological Society Special Publications, 328, 569-586 DOI: 10.1144/SP328.23

Aydin, A. & DeGraff, J. M. (1988). Evolution of polygonal fracture patterns in lava flows. Science, 239, 441-532

Bader, R. G., Gerard, R. D., Benson, W.E., Bolli, H.M., Hay, W.W., Rothwell, W.T., et al. (1970). Initial Reports of the Deep Sea Drilling Project, Site 30. Ocean Drilling Program, College Station, TX. doi:10.2973/dsdp.proc.4.1970

Beck, C., Ogawa, Y., & Dolan, J. (1990). Eocene paleogeography of the southeastern Caribbean: relations between sedimentation on the Atlantic abyssal plain at site 672 and evolution of the South America margin. In: Mascle, A., & Moore, J.C. (Eds.), Proc. ODP, Sci. Results, 110. Ocean Drilling Project, College Station, TX, 7-15

Berndt, C., Jacobs, C., Evans, A., Gay, A., Elliott, G., Long, et al. (2012). Kilometre-scale polygonal seabed depressions in the Hatton Basin, NE Atlantic Ocean: Constraints on the origin of polygonal faulting. Marine Geology 332–334, 126–133

Boschman, L. M., van Hinsbergen, D. J., Torsvik, T. H., Spakman, W., & Pindell, J. L. (2014). Kinematic reconstruction of the Caribbean region since the Early Jurassic. Earth-Science Reviews, 138, 102–136.

Boucard, M., Marcaillou, B., Lebrun, J-F., Laurencin, M., Klingelhoefer, F., Laigle, M., et al. (2021). Paleogene V-shaped basins and Neogene subsidence of the Northern Lesser Antilles Forearc. Tectonics, 40, e2020TC006524. https://doi.org/10.1029/2020TC006524

Bouysse, P., Andreieff, P., Richard, M., Baudron, J., Mascle, A., Maury, R., et al. (1985). Aves swell and northern Lesser Antilles rodge: Rock-dredging results from ARCANTE 3 cruise. In Mascle, A. (Ed.), Caribbean geodynamics. Paris: Editions Technip. 65–76

Bouysse, P., (1988). Opening of the Grenada backarc basin and evolution of the Caribbean Plate during the Mesozoic and early Paleogene: Tectonophysics, 149(1-2), 121-143

Bouysse, P., & Westercamp, D. (1990). Subduction of Atlantic aseismic ridges and Late Cenozoic evolution of the Lesser Antilles island arc. Tectonophysics, 175, 349–380.

Bowles, F. A. & Fleischer, P. (1985). Orinoco and Amazon river sediment input to the eastern Caribbean Sea. Marine Geology, 68, 53-72.

Brunet, M., Le Friant, A., Boudon, G., Lafuerza, S., Talling, P., Hornbach, M., et al., and the IODP Expedition 340 Science Party (2016). Composition, geometry, and emplacement dynamics of a large volcanic island landslide offshore Martinique: from volcano flank-collapse to seafloor sediment failure? Geochemistry, Geophysics, Geosystems, 17(3), 699–724. DOI: 10.1002/2015GC006034

Bureau, D., Mourgues, R., Cartwright, J., Foschi, M., Abdelmalak, M. M. (2013). Characterization of interactions between a pre-existing polygonal fault system and sandstone intrusions and the determination of paleo-stresses in the Faroe-Shetland basin. Journal of Structural Geology, 46, 186-199. DOI: 10.1016/j.jsg.2012.09.003

586 Carey, S. & Sigurdsson, H. (1978). Deep-sea evidence for distribution of tephra from the mixed magma
587   eruption of the Soufriere of St. Vincent, 1902: ash turbidites and air fall. Geology, 6, 271-74

588 Carey, S. & Sigurdsson, H. (1980). The Roseau Ash: deep-sea tephra deposits from a major eruption on
589   Dominica, Lesser Antilles Arc. Journal of Volcanology and Geothermal Research, 7, 67–86

590 Carey, S. & Sigurdsson, H. (1984). A model of volcanogenic sedimentation in marginal basins. Geological
591   Society Special Publication, 16, 37–58

592 Cartwright, J. A. (1994). Episodic basin-wide hydrofracturing of overpressured Early Cenozoic mudrock
593   sequences in the North Sea Basin. Marine and Petroleum Geology, 11 (5), 587–607

594 Cartwright, J. & Lonergan, L. (1996). Volumetric contraction during the compaction of mudrocks: a
595   mechanism for the development of regional-scale polygonal fault systems. Basin Research, 8, 183–193

596 Cartwright J. (2011). Diagenetically induced shear failure of fine-grained sediments and the development of
597   polygonal fault systems. Marine and Petroleum Geology, 28(9), 1593–610

598 Christeson, G. L., Mann, P., Escalona, A., & Aitken, T.J. (2008), Crustal structure of the Caribbean–
599   northeastern South America arc-continent collision zone. Journal of Geophysical Research, 113, B08104,
600   doi:10.1029/2007JB005373

601 Clausen, J. A., & Korstgård, J. A. (1993). Small scale faulting as an indicator of deformation mechanism in
602   the Tertiary sediments of the northern Danish Central Trough. Journal of Structural Geology, 15, 1343–
603   1358

604 Clausen, J.A., Gabrielsen, R.H., Reksnes, P.A., Nysaether, E. (1999). Development of intraformational
605   (Oligocene–Miocene) faults in the northern North Sea: influence of remote stresses and doming of
606   Fennoscandia. Journal of Structural Geology, 21 (10), 1457–1475. doi: 10.1016/S0191-8141(99)00083-
607   8

608 Cornée, J-J., BouDagher-Fadel, M., Philippon, M., Léticée, J-L., Legendre, L., Maincent, G., et al. (2020).
609   Paleogene carbonate systems of Saint Barthélemy, Lesser Antilles: stratigraphy and general organization.
610   Newsletters on Stratigraphy, doi:10.1127/nos/2020/0587

611 Cornée, J-J., Münch, P., Philippon, M., BouDagher-Fadel, M., Quillévéré, F., Melinte-Dobrinescu, M., et al.,
612   and the GARANTI and ANTITHESIS Scientific Parties (2021). Lost islands in the northern Lesser
613   Antilles: a possible milestone in the Cenozoic dispersal of terrestrial organisms between South-America
614   and the Greater Antilles. Earth Sciences Reviews. Accepted

615 Corredor, J., Moreli, J., Lopez, J., Capella, J., Armstrong, R. (2004). Cyclonic eddy entrains Orinoco river
616   plume in Eastern Caribbean. EOS Transactions – American Geophysical Union 85 (20), 197–201

617 Cosgrove, J. (1995). The expression of hydraulic fracturing in rocks and sediments, Geological Society Special
618   Publication, 92, 187–196

619 Davies, R. J., Ireland, M. T., & Cartwright, J. (2009). Differential compaction due to irregular topology of a
620   diagenetic reaction boundary: a new mechanism for the formation of polygonal faults. Basin Research,
621   21, 354–359

DeMets, C., Jansma, P. E., Mattioli, G. S., Dixon, T. H., Farina, F., Bilham, R., et al. (2000). GPS geodetic constraints on Caribbean-North America plate motion. Geophysical Research Letters, 27(3), 437–440. https://doi.org/10.1029/1999GL005436

Deplus, C., Le Friant, A., Boudon, G., Komorowski, J-C., Villemant, B., Harford, C. et al. (2001). Submarine evidence for large-scale debris avalanches in the Lesser Antilles Arc. Earth and Planetary Science Letters, 192(2), 145-157. DOI: 10.1016/S0012-821X(01)00444-7

Desprairies, A. & Bonnot-Courtois, C. (1980). Relation entre la composition des smectites d'altération sous-marine et leurs cortèges de terres rares. Earth and Planetary Science Letters, 48(1), 124-130

Deville, E., Mascle, A., Callec, Y., Huyghe, P., & Lallemant, S. (2015). Tectonics and sedimentation interactions in the east Caribbean subduction zone; an overview from the Orinoco Delta and the Barbados accretionary prism. Marine and Petroleum Geology, 64, 76-103. DOI: 10.1016/j.marpetgeo.2014.12.015

Dewhurst, D. N., Cartwright, J., Lonergan, L. (1999). The development of polygonal fault systems by syneresis of colloidal sediments. Marine and Petroleum Geology, 16, 793–810

Diaz de Gamero, M. L. (1996). The changing course of the Orinoco river during the neogene: a review. Palaeogeography, Palaeoclimatology, Palaeoecology, 123, 385–402

Earl, E. (1997). Assessment of the behaviour of field soils during compression. Journal of Agricultural Engineering Research, 68, 147–157

Escalona, A., & Mann, P. (2010). Tectonics, basin subsidence mechanisms, and paleogeography of the Caribbean-South American plate boundary zone. Marine and Petroleum Geology, 28, 8–39. https://doi.org/10.1016/j.marpetgeo.2010.01.016

Feuillet, N., Leclerc, F., Tapponnier, P., Beauducel, F., Boudon, G., Le Friant, A., et al. (2010). Active faulting induced by slip partitioning in Montserrat and link with volcanic activity: New insights from the 2009 GWADASEIS marine cruise data. Geophysical Research Letters, 37, L00E15. https://doi.org/10.1029/2010GL042556

Forsberg, C. F., & Locat, J. (2005). Mineralogical and microstructural development of the sediments on the Mid-Norwegian margin. Marine and Petroleum Geology, 22 (1–2), 109–122

Fox, P. J., Schreiber, E., & Heezen, B. C. (1971). The geology of the Caribbean crust: Tertiary sediments, granitic and basic rocks from the Aves Ridge. Tectonophysics, 12(2), 89–109

Garrocq, C., Lallemand, S., Marcaillou, B., Lebrun, J-F., Padron, C., Klingelhoefer, F., et al., and the GARANTI cruise team (2020). Genetic relations between the Aves Ridge and the Grenada back-arc basin, East Caribbean Sea. Journal of Geophysical Research: Solid Earth, 126, e2020JB020466. https://doi.org/10.1029/2020JB020466

Gay, A., Lopez, M., Cochonat, P., & Sermondadaz, G. (2004). Polygonal faults–furrows system related to early stages of compaction — Upper Miocene to present sediments of the Lower Congo Basin. Basin Research, 16, 101–116

Gay, A., & Berndt, C. (2007). Cessation/reactivation of polygonal faulting and effects on fluid flow in the Vøring Basin, Norwegian Margin. Journal of the Geological Society of London, 164, 129–141

659   Ghalayini, R., & Eid, C. (2020). Using polygonal layer-bound faults as tools to delimit clastic reservoirs in the
660   Levant Basin offshore Lebanon. AAPG Bulletin, 104(3), 629-656. DOI: 10.1306/07151918155

661   Gómez-García, Á. M., Meeßen, C., Scheck-Wenderoth, M., Monsalve, G., Bott, J., Bernhardt, A. et al. (2019).
662   3D Modeling of Vertical Gravity Gradients and the Delimitation of Tectonic Boundaries: The Caribbean
663   Oceanic Domain as a Case Study: Geochemistry, Geophysics, Geosystems, 20(11), 5371-5393

664   Goulty, N. R. (2002). Mechanics of layer-bound polygonal faulting in fine-grained sediments. Journal of the
665   Geological Society of London, 159, 239–246

666   Goulty, N. R. (2008). Geomechanics of polygonal fault systems: a review. Petroleum Geoscience, 14, 389–
667   397

668   Hansen, D. M., Shimeld, J. W., Williamson, M. A., & Lykke-Andersen, H. (2004). Development of a major
669   polygonal fault system in Upper Cretaceous chalk and Cenozoic mudrocks of the Sable Subbasin,
670   Canadian Atlantic margin. Marine and Petroleum Geology, 21, 1205–1219

671   Hansen, J. P. V., Cartwright, J. A., Huuse, M., & Clausen, O. R. (2005). 3D seismic expression of fluid
672   migration and mud remobilization on the Gjallar Ridge, offshore mid-Norway. Basin Research, 17, 123–
673   139

674   He, C., Tang, C., Huang, D., & Shi, S., (2010). Polygonal faults in the Sanzhao sag of the Songliao basin: their
675   significance in hydrocarbon accumulation. Mining Science and Technology, 20, 300–305

676   Ho, S., Hovland, M., Blouet, J-P., Wetzel, A., Imbert, P., & Carruthers, D. (2018). Formation of linear
677   planform chimneys controlled by preferential hydrocarbon leakage and anisotropic stresses in faulted
678   fine-grained sediments, offshore Angola. Solid Earth, 9, 1437-1468. https://doi.org/10.5194/se-9-1437-
679   2018

680   Holcombe, T. L., Ladd, J. W., Westbrook, G., Edgar, N. T., & Bowland, C. L. (1990). Caribbean marine
681   geology; ridges and basin of the plate interior. In: Dengo, G., Case, J. E.(Eds.), The Caribbean Region,
682   the Geology of North America. Geological Society of America, Boulder, CO, 231-260

683   Ireland, M. T., Davies, R. J., Goulty, N. R., & Carruthers, D. (2011). Structure of a silica diagenetic
684   transformation zone: the Gjallar Ridge, offshore Norway. Sedimentology, 58, 424–441

685   Iturralde-Vinent, M. A. & MacPhee R. D. E. (1999). Paleogeography of the Caribbean region: implications
686   for Cenozoic biogeography. Bulletin of the American Museum of Natural History, 95p

687   Jackson, C., Carruthers D., Mahlo S., & Briggs O. (2014). Can polygonal faults help locate deep-water
688   reservoirs? AAPG Bulletin, 98(9), 1717–1738

689   James, D. M. D. (2006). Discussion on development of polygonal fault systems: a test of hypotheses. Journal
690   of the Geological Society of London, 162, 587–590

691   Jany, I., Scanlon, K. M., & Mauffret, A. (1990). Geological interpretation of combined seabeam, gloria and
692   seismic data from Anegada passage (Virgin Islands, north Caribbean). Marine Geophysical Researches,
693   12, 173-196

694 Jitmahantakul, S., Chenrai P., Kanjanapayont P., & Kanitpanyacharoen W. (2020). Seismic characteristics of
695   polygonal faults systems in the Great South Nasin, New Zealand. Open Geosciences, 12, 851-865.
696   https://doi.org/10.1515/geo-2020-0177

697 Kinder, T. H., Heburn, G. W., & Green, A. W. (1985). Some aspects of the Caribbean circulation. Marine
698   Geology, 68, 25-52

699 Klitgord, K. D. & Grow, J. A. (1980) Jurassic seismic stratigraphy and basement structure of the western
700   Atlantic magnetic quiet zone. AAPG Bulletin, 64, 1658-1680

701 Lachenbruch, A. H. (1962). Mechanics of thermal contraction cracks and ice-wedge polygons. GSA Special
702   Paper, 70

703 Ladd, J. W., & Sheridan, R. E. (1987). Seismic stratigraphy of the Bahamas. AAPG Bulletin, 71(6), 719–736

704 Laurent, D., Gay A., Baudon C., Berndt C., Soliva R., Planke S., et al. (2012). High-resolution architecture of
705   a polygonal fault interval inferred from geomodel applied to 3D seismic data from the Gjallar Ridge,
706   Vøring Basin, Offshore Norway. Marine Geology, 332, 134-151

707 Lebrun, J-F., & Lallemand, S. (2017). GARANTI cruise, L'Atalante R/V. https://doi.org/10.17600/17001200

708 Le Friant, A., Lebas, E., Brunet, M., Lafuerza, S., Hornbach, M., Coussens, et al., and the IODP 340 Expedition
709   Science Party (2020). Submarine landslides around volcanic islands: a review of what can be learned from
710   the Lesser Antilles Arc. In Ogata, K., Festa, A., and Pini, G. A. (Eds.), Submarine Landslides: Subaqueous
711   Mass Transport Deposits from Outcrops to Seismic Profiles. Geophysical Monograph, 246, 277–297.
712   https://doi.org/10.1002/9781119500513.ch17

713 Legendre, L., Philippon, M., Münch, P., Leticee, J-L., Noury, M., Maincent, G., et al. (2018). Trench bending
714   initiation: Upper plate strain pattern and volcanism. Insights from the Lesser Antilles arc, St. Barthelemy
715   Island, French West Indies. Tectonics, 37(9), 2777-2797

716 Li, J., Mitra, S., & Qi, J. (2020). Seismic analysis of polygonal fault systems in the Great South Basin, New
717   Zealand. Marine and Petroleum Geology, 111, 638-649. https://doi.org/10.1016/j.marpetgeo.2019.08.052

718 Lonergan, L., Cartwright, J., & Jolly, R. (1998). The geometry of polygonal fault in Tertiary mudrocks of the
719   North Sea. Journal of Structural Geology, 20, 529–548

720 Macdonald R., Hawkesworth C.J. & Heath E. (2000). The lesser Antilles chain: a study in arc magmatism.
721   Earth Science Reviews, 49 (1), 1-76

722 MacPhee, R. D. E., Ford D. C., & McFarlane D. A. (1989). Pre-Wisconsinan mammals from Jamaica and
723   models of late Quaternary extinction in the Greater Antilles. Quaternary Research, 31(1), 94-106

724 Mann, P., Taylor F.W., Edwards L. R. & Ku, T-L. (1995). Actively evolving microplate formation by oblique
725   collision and sideways motion along strike-slip faults: an example from the northeastern Caribbean plate
726   margin. Tectonophysics, 246, 1–69

727 Mann, P. (1999). Caribbean sedimentary basins: Classification and tectonic setting from Jurassic to present.
728   In Mann, P. (Ed), Caribbean Basins: Sedimentary Basins of the World, vol. 4, Chapter 1. Elsevier Science,
729   B.V., Amsterdam. DOI: 10.1016/S1874-5997(99)80035-5

730   Mas, A., Patrier P., Beaufort D. & Genter A. (2003). Clay-mineral signatures of fossil and active
731   hydrothermal circulations in the geothermal system of the Lamentin Plain, Martinique. Journal of
732   Volcanology and Geothermal Research, 124, 195-218.

733   Mas, A., Guisseau D., Patrier P., Beaufort D. Genter A., Sanjuan, B. et al. (2006). Clay minerals related to
734   the hydrothermal activity of the Bouillante geothermal field (Guadeloupe). Journal of Volcanology and
735   Geothermal Research, 158, 380-400.

736   Morley, C.K. & Binazirnejad, H. (2020). Investigating polygonal fault topological variability: Structural
737   causes vs image resolution. Journal of Structural Geology, 130, 103930.
738   https://doi.org/10.1016/j.jsg.2019.103930

739   Müller, R. D., Zahirovic, S., Williams, S.E., Cannon, J., Seton, M., Bower, D.J. et al. (2019). A Global Plate
740   Model Including Lithospheric Deformation Along Major Rifts and Orogens Since the Triassic. Tectonics,
741   38, 1884–1907. https://doi.org/10.1029/2018TC005462

742   Münch, P., Cornee, J-J., Lebrun, J-F., Quillevere, F., Verati, C., Melinte-Dobrinescu, M., et al. (2014). Pliocene
743   to Pleistocene vertical movements in the forearc of the Lesser Antilles subduction: Insights from
744   chronostratigraphy of shallow-water carbonate platforms (Guadeloupe archipelago). Journal of the
745   Geological Society, 171(3), 329–341

746   Murray, N. A., McManus, J., Palmer, M. R., Haley, B., & Manners, H. (2018). Diagenesis in tephra-rich
747   sediments from the Lesser Antilles Volcanic Arc: pore fluid constraints. Geochimica et Cosmochimica
748   Acta, 228, 119-35. DOI: 10.1016/j.gca.2018.02.039

749   Neagu, R. C., Cartwright, J., & Davies, R. J. (2010). Measurement of diagenetic compaction strain quantitative
750   analysis of fault plane dip. Journal of Structural Geology, 32, 641–655

751   Neill, I., Kerr, A. C., Hastie, A. R., Stanek, K. P., & Millar, I. L. (2011). Origin of the Aves Ridge and Dutch–
752   Venezuelan Antilles: Interaction of the Cretaceous 'Great Arc' and Caribbean–Colombian Oceanic
753   Plateau? Journal of the Geological Society, 168(2), 333–348

754   Oldham, A. C. & Gibbins, N. M. (1995). Lake Hope 3D: a case study. Exploration Geophysics, 26, 383-394

755   Padron, C., Klingelhoefer, F., Marcaillou, B., Lebrun, J-F., Lallemand, S., Garrocq, C., et al. (2021). Deep
756   structure of the Grenada Basin from wide-angle seismic, bathymetric and gravity data. Journal of
757   Geophysical Research: Solid Earth, 126, e2020JB020472. https://doi.org/10.1029/2020JB020472

758   Parra, M., Delmont, P., Ferragne, A., Latouche, C., Pons, J. C. & Puechmaille, C, (1985). Origin and evolution
759   of smectites in recent marine sediments of the NE Atlantique. Clay Minerals, 20, 335-346

760   Parra, M., Pons, J.C., & Ferragne, A. (1986). Two potential sources for Holocene clay sedimentation in the
761   Caribbean Basin: The Lesser Antilles Arc and the South American continent. Marine Geology, 72(287),
762   3-14. DOI: 10.1016/0025-3227(86)90124-6

763   Pautrizel, F. & Pons, J.-C. (1981). Modalités de la sédimentation au Quaternaire récent dans la Mer des Petites
764   Antilles (Fosse de Grenade--Ride des Oiseaux--Bassin du Venezuela). Bulletin lnstitut Géologie Bassin
765   Aquitaine, 30, 239-262

766 Petracchini, L., Antonellini, M., Billi, A., & Scrocca, D. (2015). Syn-thrusting polygonal normal faults exposed
767   in the hinge of the Cingoli anticline, northern Apennines, Italy. Frontiers in Earth Sciences, 3, 67. doi:
768   10.3389/feart.2015.00067

769 Philippon, M., Cornée, J-J., Münch, P., van Hinsbergen, D. J. J., BouDagher-Fadel, M., Gailler, L., et al.
770   (2020a). Eocene intra-plate shortening responsible for the rise of a faunal pathway in the northeastern
771   Caribbean realm. PLoS One, 15(10), e0241000. https://doi.org/10.1371/journal.pone.0241000

772 Philippon M., van Hinsbergen, D., Boschman, L.M., Gossink, L., Cornée, J-J., BouDagher-Fadel, M., et al.
773   (2020b). Caribbean intra-plate deformation: Paleomagnetic evidence from St. Barthelemy island for Post-
774   Oligocene rotation in the Lesser Antilles forearc. Tectonophysics, 777, 228323.

775 Picard, M., Schneider, J-L., Boudon, G., & Mulder, T. (2006). Contrasting sedimentary processes along a
776   convergent margin; the Lesser Antilles arc system. Geo-Marine Letters, 26(6), 397-410. DOI:
777   10.1007/s00367-006-0046-y

778 Pindell, J. L. & Barrett, S. F. (1990). Geological evolution of the Caribbean region: a plate tectonic perspective.
779   In: Dengo, G., Case, J. E. (Eds.), The Caribbean Region, the Geology of North America. Geological
780   Society of America, Boulder, CO, 405–432

781 Pindell, J., Kennan, L., Stanek, K.P., Maresch, W.V., & Draper, G. (2006). Foundations of Gulf of Mexico
782   and Carribean evolution : eight controversies resolved. Geologica Acta, 4 (1-2), 303-341

783 Pindell, J. L., & Kennan, L. (2009). Tectonic evolution of the Gulf of Mexico, Caribbean and northern South
784   America in the mantle reference frame: An update. Origin and Evolution of the Caribbean Plate, 328(1),
785   1–55. https://doi.org/10.1144/sp328.1

786 Pindell, J., Maresch, W. V., Martens, U., & Stanek, K. (2012). The Greater Antillean Arc: Early Cretaceous
787   origin and proposed relationship to Central American subduction mélanges: Implications for models of
788   Caribbean   evolution.   International   Geology   Review,   54(2),   131–143.
789   https://doi.org/10.1080/00206814.2010.510008

790 Ramsay J. G. (1967). Folding and Fracturing of Rocks, New York, 1967, 568 pp

791 Reiche, S., Hjelstuen, B. O., & Haflidason, H. (2011). High-resolution seismic stratigraphy, sedimentary
792   processes and the origin of seabed cracks and pockmarks at Nyegga, mid-Norwegian margin. Marine
793   Geology, 284(1), 28–39

794 Seibert, C., Feuillet, N., Ratzov, G., Beck, C., & Cattaneo, A. (2020). Seafloor morphology and sediment
795   transfer in the mixed carbonate siliciclastic environment of the Lesser Antilles forearc along Barbuda to
796   St. Lucia. Marine Geology, 428, 106242

797 Sen Gupta, B. K., Temples, T.J., & Dallmeyer, M. D. G. (1982). Diagenesis in tephra-rich sediments from the
798   Lesser Antilles volcanic arc; pore fluid constraints. Marine Micropaleontology, 7(4), 297-309

799 Shin, H., Santamarina, J. C., & Cartwright, J. A. (2008). Contraction-driven shear failure in compacting
800   uncemented sediments. Geology, 36(12), 931–934

801 Shin, H., Santamarina, J. C., & Cartwright, J. A. (2010). Displacement field in contraction driven faults.
802   Journal of Geophysical Research, 115(B7), 13. http://dx.doi.org/10.1029/2009JB006572

803   Sigurdsson, H., Sparks, R. S. J., Carey, S.T., & Huang, T. C. (1980). Volcanogenic sedimentation in the Lesser
804   Antilles arc. Journal of Geology, 88, 523–540

805   Speed, R. C., & Westbrook, G. K. (1984). Lesser Antilles arc and adjacent terranes. In Atlas 10, ocean margin
806   drilling program (Marine Science International).MA: Woods Hole.

807   Sun, Q., Wu, S., Lü, F., & Yuan, S. (2010). Polygonal faults and their implications for hydrocarbon reservoirs
808   in the southern Qiongdongnan Basin, South China Sea. Journal of Asian Earth Sciences, 39, 470–479

809   Tuckwell, G. W., Lonergan, L. & Jolly, R. (2003). The control of stress history and flaw distribution on the
810   evolution of polygonal fracture networks. Journal of Structural Geology, 25, 1241–1250

811   Waldron J. W. F. (1988). Determination of finite strain in bedding surfaces using sedimentary structures and
812   trace fossils: a comparison of techniques. Journal of Structural Geology, 10, 273-281

813   Watterson, J., Walsh, J., Nicol, A., Neil, P. A. R., & Bretan, P. G. (2000). Geometry and origin of a polygonal
814   fault system. Journal of the Geological Society of London, 157, 151–162

815   Weinberger, R. (1999). Initiation and growth of cracks during desiccation of stratified muddy sediments.
816   Journal of Structural Geology, 21, 379-386.

817   Wrona T., Magee C., Jackson C., Huuse M., & Taylor, K. (2017). Kinematics of polygonal fault systems:
818   Observations from the Northern North Sea. Frontiers in Earth Sciences, 5, 101
819   https://doi.org/10.3389/feart.2017.00101

820   Ysaccis, R. (1997). Tertiary evolution of the northeastern Venezuela offshore (Thesis). Rice University,
821   Houston, TX. Retrieved from https://scholarship.rice.edu/handle/1911/1933